

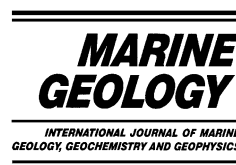


ELSEVIER

Available online at www.sciencedirect.com

SCIENCE @ DIRECT®

Marine Geology 203 (2004) 119–140



www.elsevier.com/locate/margeo

Evidence for hydrothermal venting and sediment volcanism discharged after recent short-lived volcanic eruptions at Deception Island, Bransfield Strait, Antarctica

L. Somoza^{a,*}, J. Martínez-Frías^b, J.L. Smellie^c, J. Rey^d, A. Maestro^a

^a *Marine Geology Division, Geological Survey of Spain, IGME, Ríos Rosas, 23, 28003 Madrid, Spain*

^b *Centro de Astrobiología, CSIC/INTA, Torrejón de Ardoz, E-28850 Madrid, Spain*

^c *British Antarctic Survey, High Cross, Madingley Road, Cambridge, CB3 0ET, UK*

^d *Estudios Geológicos Marinos ESGEMAR, Espacio, 4, 29006 Málaga, Spain*

Received 19 July 2002; received in revised form 26 May 2003; accepted 17 June 2003

Abstract

The results of a combined geophysical and geochemical research programme on Deception Island, an active volcano at 62°43'S, 60°57'W in Bransfield Strait (Antarctica), are presented. Ultrahigh-resolution acoustic data obtained with a TOPAS (TOPographic PARAMeter Sonar) system and multibeam bathymetry (Simrad EM1000) allow a detailed analysis of submarine vents in Port Foster, the submerged caldera of Deception Island. The data show three different types of seafloor structures: low-relief mounds, high-relief mounds ('wasp nest'-like) and spire-like structures. We interpret these structures as products of sediment volcanism and seeps caused by heating and boiling of pore fluids in gas-charged sediments, and related to recent short-lived volcanic events, possibly those that occurred in 1967, 1969 and 1970. In addition, subsurface vertical disturbed zones, formed by increased amplitude and phase-inverse reflectors beneath the mounds, suggest the presence of fluidised and brecciated sediments within hydrofracture systems. A key finding of this study is that there appears to be a close relationship between the submarine mounds detected by our ultrahigh-resolution seismic study, geochemical haloes, fault-pathways and present-day thermal anomalies in surface waters. We suggest that seafloor hydrofracture systems and subsurface pipes can be re-used as fluid migration pathways, resulting in hydrothermal seeps and vents on the seafloor, possibly up to decades after coeval volcanic eruptions.

© 2003 Elsevier B.V. All rights reserved.

Keywords: hydrothermal vents; submarine volcanoes; geophysical surveys; geochemical investigations; Antarctica

1. Introduction

Seafloor hydrothermal fields are hosted world-

wide by large volcanic systems found in both fast and slow oceanic spreading centres and back-arc basins (German et al., 1995). Most of the available information about seafloor hydrothermal processes has been based on sampling fluids and dispersed plumes from vent emissions at deep-sea oceanic spreading systems (Parson et al., 1995). In

* Corresponding author. Tel.: +34-91-7287230.

E-mail address: l.somoza@igme.es (L. Somoza).

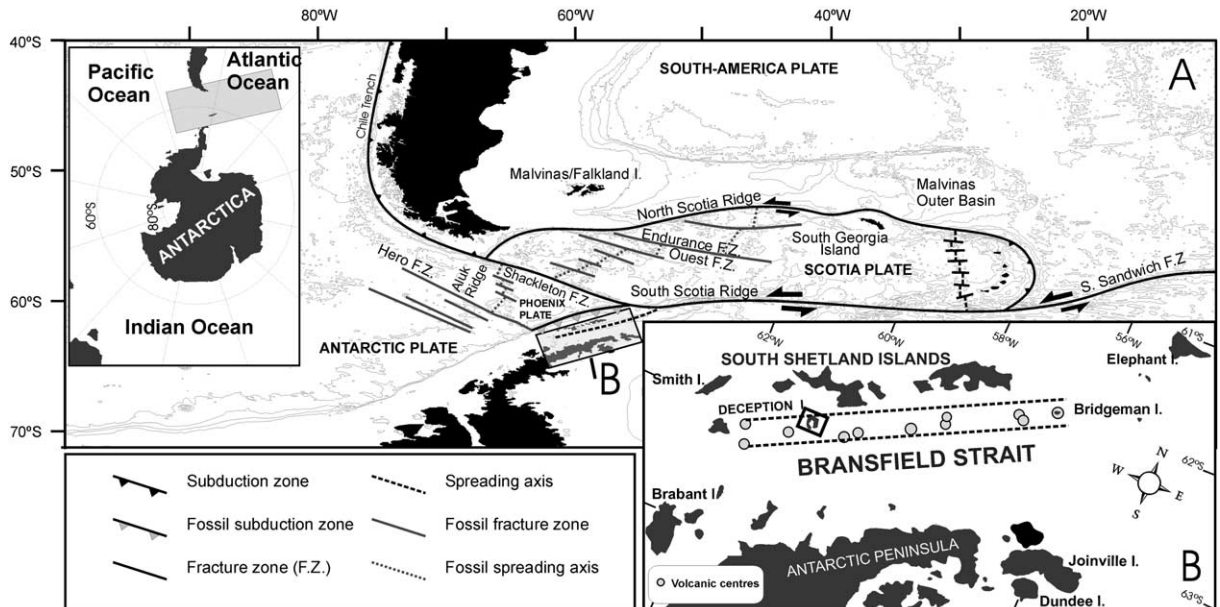


Fig. 1. (A) Map showing the regional tectonic setting with major convergent and divergent plate boundaries of the Scotia Sea between South America and the Antarctic Peninsula. Modified after the British Antarctic Survey (BAS, 1985). (B) Map showing the location of Deception Island and other volcanic centres (mainly submarine) in Bransfield Strait.

contrast, shallow-water boiling systems show differences from typical deep-sea hydrothermal vents caused by lower confining pressures that are no longer sufficient to maintain superheated fluids as a single phase (Hannington et al., 2001). At reduced pressures, phase separation of the fluid occurs, resulting in a dense brine-type phase and a low-salinity, relatively metal-free vapour-rich phase (Massoth et al., 1989). The hydrothermal systems are profoundly altered by magmatic intrusions, generating episodic fluctuations and short-lived events (Butterfield et al., 1997). Examples of hydrothermal fields perturbed by magmatic intrusions show that fluids discharged after a sudden magmatic intrusion, may be altered by phase separation in the fluids. Following magma emplacement, fluids may be stored in the crust and flushed years later by convecting seawater (Butterfield et al., 1994; Baker, 1995). Simultaneously, episodic short-lived magmatic intrusions produce significant changes in rare earth element (REE) patterns which are caused by the prevailing

chemical and temperature conditions in the hydrothermal system(s) (Butterfield and Massoth, 1994; Klinkhammer et al., 1994).

Deception Island ($62^{\circ}43'S$, $60^{\circ}57'W$) is an active basalt–andesite volcano in Bransfield Strait, Antarctica (Fig. 1). Its geology and volcanic evolution are described in detail by Smellie et al. (2002). Eruptions were frequent during the eighteenth and nineteenth centuries, but infrequent in the twentieth century. The volcano contains a ring-shaped volcanic caldera 8–10 km in diameter, which is restless and may be resurging (Cooper et al., 1998). It is flooded by the sea (Port Foster) and has a maximum water depth of about 167 m at its centre (Fig. 2). In this paper, we present the results of geophysical and geochemical studies of shallow-water hydrothermal vents at Deception Island. Our work demonstrates the importance of understanding volcano–tectonic processes in modern caldera-related settings, and it provides insights into the timing and location of putative ore bodies.

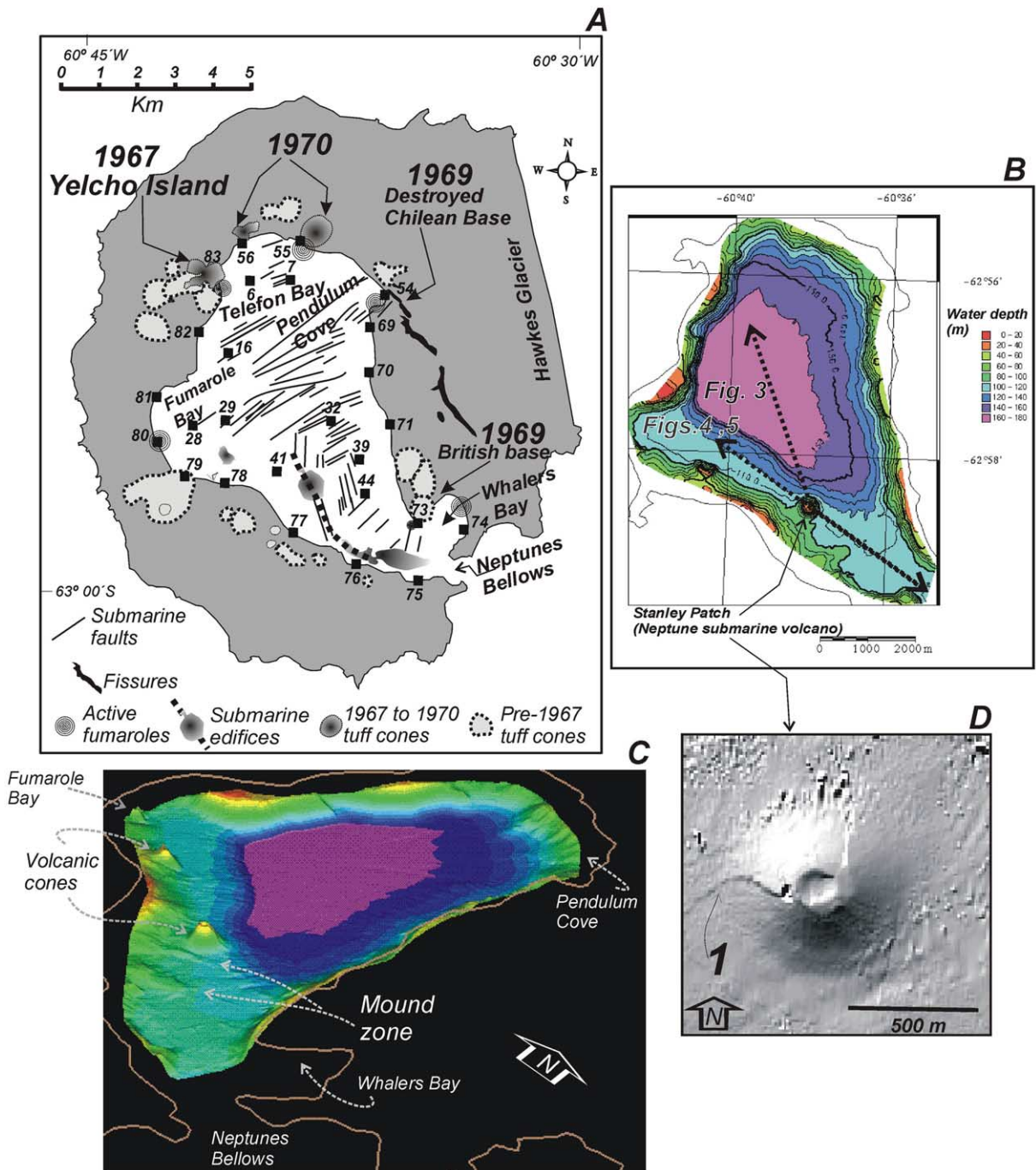


Fig. 2. (A) Map showing the main tectonic, volcanic and hydrothermal features of Deception Island and positions of the sampling stations. Submarine structures and faults are partly modified from Rey et al. (1995, 2002). (B) Bathymetry of the submerged caldera of Deception Island based on multibeam data, with location of seismic profiles shown in Figs. 3–5. (C) 3-D image of the submerged caldera. Oblique view looking northwest. The mound zone is located southeast of Stanley Patch ('Neptune submarine volcano'; see also Figs. 4–6). (D) Shaded relief of Stanley Patch, based on multibeam bathymetric data, showing vent fissures (1) on the flanks of the cone-shaped edifice. The image is illuminated from the northwest.

2. Regional setting

2.1. Geodynamic framework

Deception Island is located at the southwestern end of Bransfield Strait, an actively extending young (probably < 4 Ma old; Barker, 1982) marginal basin between the Antarctic Peninsula and South Shetland Islands (Fig. 1). Deception Island is the most active of several volcanoes situated in Bransfield Strait (Smellie, 1990; Lawver et al., 1995). A multibeam bathymetric chart of Bransfield Strait (Lawver et al., 1996; Gracia et al., 1996) shows a series of circular submarine volcanoes and aligned basaltic ridges between the two largest volcanic islands, Deception Island and Bridgeman Island. Dredge samples taken from the submarine linear ridges in the Bransfield Strait have been reported as fresh, glassy vesicular basalt with a chemistry similar to Lau Basin and other Pacific back-arc basin basalts (Keller et al., 2002).

This volcanic ridge has traditionally been interpreted as a Late Cenozoic tensional structure produced as a consequence of back-arc spreading (Roach, 1978; Peccerillo et al., 1991) linked to subduction of the Phoenix Plate beneath the Antarctic Plate (González-Ferrán, 1985). Island arc volcanism in the South Shetland Islands has occurred in several pulses since Early Cretaceous times, with the last eruptive period 20–30 m.y. ago (Pankhurst and Smellie, 1983; unpublished data of J.L.S.). It has been proposed that the former Phoenix Plate and the Bransfield Basin became part of the Antarctic Plate when seafloor spreading stopped at the Aluk Ridge at 4 Ma and subduction at the South Shetland Trench ceased (Barker, 1982; Livermore et al., 2000). Lawver et al. (1996) proposed that opening of Bransfield Strait is not produced by typical back-arc extension associated with active subduction, but is a product of the combined effect of the continued sinking of the slab, associated rollback movement and minor extension accompanied by fracturing, which allowed magmatic intrusions to be emplaced into an extended continental margin. Although Deception Island is situated close to a postulated axis of spreading, the presence of

underlying arc-type basement rather than proto-ocean floor (Smellie et al., 1992; Risso and Aparicio, 2002) is confirmation of an extended continental margin setting. The development of Bransfield Strait has also been related to a sinistral simple-shear couple between the Scotia and Antarctic plates (Fig. 1), which displaced the former Phoenix Plate toward the northwest (Rey and Somoza, 1992; Barker and Austin, 1994; González-Casado et al., 2000). This regional stress field has also been proposed to explain the recent tectono-magmatic evolution of Deception Island (Rey et al., 1995).

2.2. Hydrothermal activity in the Bransfield Strait

Evidence for hydrothermal activity in Bransfield Strait was first reported in sediments of the Eastern King George Basin, where thermogenic hydrocarbons generated by low temperature (< 150°C), hydrothermal interaction between organic rich sediments and fluid advected from deeper levels were detected (Suess et al., 1987). Further evidence comes from $\delta^3\text{He}$ values in the water column (Schloesser et al., 1988). High crustal heat flow was detected in the centre of Bransfield Strait, with values typical of regions with active hydrothermal circulation (Lawver et al., 1995). New hydrothermal vent sites have recently been discovered at Hook Ridge, a volcanic edifice in the Central Bransfield Basin (Klinkhammer et al., 2001). Native sulphur, Fe-sulfides, and hydrothermal barites were recovered and phase separation was suggested to be a control on the chemistry of the venting fluids (Dähmann et al., 2001).

3. Background information

3.1. Recent volcanic eruptions

Four recent volcanic events, which occurred in 1967, 1969, 1970 (Orheim, 1972), and 1987 (LeMasurier and Thomson, 1990), have been reported for Deception Island. In December 1967, violent tremors and explosions occurred in Telefon Bay (Fig. 2A). The volcanic event formed Yelcho Island, which measured 934 m in length

next to 366 m in width and reached 62 m above sea level and was composed of three collinear craters (Baker et al., 1975). During the eruption, the sea within Pendulum Cove began to boil and a strong odour of sulphur was detected (Valenzuela et al., 1968). Gallardo et al. (1999) found that the structure and composition of the benthic community in Port Foster were altered after the 1967 eruption and attributed those changes to volcanic perturbation. In 1969, the Chilean station was completely destroyed by a combination of ashfall and mudflow during an eruption from fissures beneath the small ice cap (Baker et al., 1975). Water vapour and hydrogen sulphide gas were detected, and elemental sulphur deposited from numerous small fumaroles and vents. The British station was heavily damaged by mudflow caused by extensive melting of the ice cap (Baker et al., 1975; Smellie, 1988; Smellie, 2002a). After this event, the historically long-lived (> 200 years) fumarole activity in the Fumarole Bay area was intense with sulphur deposition along parallel tracks, and steam and boiling water (100°C) issuing at sea level. Hydrothermal/volcanic activity at Yelcho Island was accompanied by CO₂ and/or H₂S release into the crater lake. The last well-documented eruption of Deception Island, in 1970, was more violent than its predecessors in 1967 and 1969. Five maar-like submarine craters and seven land vents were created in an arcuate zone ~ 5 km long. They erupted andesitic tephra and built ~ 1.5 km² of new land in the Telefon Bay area (Baker and McReath, 1971; Baker et al., 1975). The tephra blanket was salt-rich, suggesting involvement of substantial quantities of sea water (Shultz, 1972). Deception Island has been monitored seismically every austral summer since 1986. During the austral winter of 1986–1987, infrared imagery from the 10 NOAA polar orbiting weather satellites suggested that an ash plume extended ~ 100 km SE of Deception Island, although there was no evidence that new volcanic cones formed on the island (LeMasurier and Thomson, 1990). Subsequent more accurate geolocation of the plume source showed that it was situated about 250 km NE of Deception Island, in an area not known or expected to have volcanoes,

and it appears to have been a meteorological effect (Smellie, unpublished data).

Finally, a linear magnetic anomaly interpreted as a high-level magmatic intrusion, was identified on the northeast side of Port Foster (Garcia et al., 1989). The seafloor above the intrusion has been rising at a rapid rate (ca. 0.3–0.5 m.a⁻¹ averaged over about 50 years since 1945), and is interpreted to be an indication of resurgent activity in the caldera (Cooper et al., 1998) although there have been no eruptions at that locality.

3.2. Present hydrothermal activity: fumaroles and hot springs

Subaerial fumaroles are common in several areas on and offshore at Deception Island (e.g. Fumarole Bay, Telefon Bay, Pendulum Cove, Whalers Bay; Smellie and López-Martínez, 2000). They are related to venting from shallow aquifers heated by convective gaseous inflow from an underlying magma chamber (Ramos et al., 1989). The main component of the fumarole emissions is CO₂ (75–90%) with significant proportions of H₂S (0.3–0.9%), H₂ (0.006–0.20%), N₂ (0.77–21.6%), and O₂ (0.006–0.65%), and an equilibrium formation temperature of 219°C (Valentin et al., 1989). An abrupt increase in H₂S/CO₂ ratios has been reported for periods of high frequency seismic events (Villegas and Caselli, 1995). The origin of low-frequency volcanic tremors recorded at Deception Island has been interpreted as acoustic emissions, which are interpreted as turbulent motion induced by venting from shallow aquifers to the surface (Vila et al., 1992). Temperatures as high as 107°C are recorded in beach interstitial waters close to the fumarole emissions (Villegas and Caselli, 1995; unpublished data of J.L.S.). Thermal anomalies of 7–15°C in surface waters have been measured in the small bays surrounding Port Foster, and persist as a thin surface layer to about 20–30 m offshore (Dykes et al., 2001). In Port Foster itself, seawater surface temperatures vary between 0°C and –1°C close to Neptunes Bellows and exceed 3°C in the centre of the bay (Rey et al., 1997). Acoustic Doppler current profile data indicate

that inertial and/or tidal currents within Port Foster are quite complex (Lenn et al., 2002).

3.3. Submarine and subaerial fault systems

Fault systems and fault-related subaerial and submarine volcanic cones (Fig. 2A) may be arranged in several main orientations that have been interpreted as a consequence of an extensional regional stress field (Rey et al., 1995): a NW–SE alignment exists for seafloor volcanic cones and recent subaerial tuff cones (1967 Telefon Bay eruption). This direction is parallel to the axis of a minimum magnetic anomaly, with >3000 nT decrease in the field, reported within Port Foster and interpreted to be caused by a linear magmatic intrusion (Garcia et al., 1989), and with the σ_3 regional stress direction obtained from earthquake focal mechanism studies (Pelayo and Wiens, 1980; Galindo-Zaldívar et al., 1996; González-Casado et al., 2000). A NE–SW fault system crosses Port Foster between Fumarole Bay and Pendulum Cove, and is associated with active seismic activity (Ortiz et al., 1992) and fumarole emissions at temperatures of 70–>100°C on beaches at Pendulum Cove and Fumarole Bay (Smellie, unpublished data). Horizontal polarisation analysis of low-frequency volcanic tremors recorded at Deception Island also shows azimuths of N125E and N145E (1.4 Hz) and N80E (2.0 Hz) for the main axis of the horizontal polarisation ellipsoid (Felpeto et al., 1995). N050E-trending faults related to fumarole emissions at temperatures of 40–43.5°C have also been reported at Stonethrow Ridge (López et al., 1995). This alignment may have been caused by tensional faulting along an axis of maximum shortening (Rey et al., 1997).

4. Methods and data acquisition

Our study is based on data collected from several cruises carried out in Port Foster. During cruises in the austral summers of 1987–1988 and 1988–1989, R/V *Las Palmas* completed a dense network of side-scan sonar imaging (500 kHz) and medium-resolution seismic reflection profiles

(3500–7000 Joule Sparker system, 50 Hz to 4 kHz) orientated N–S and NW–SE, with an average penetration of 500 ms (TWT time). A map of the seafloor was published by Rey et al. (1992, 2002). In addition, seafloor sediments from 54 stations were recovered using a Shipek-type sampler.

Ultrahigh-resolution seismic profiles of seafloor structures, previously observed only with medium-resolution reflection seismic profiles, were obtained with a TOPAS PS 018 Simrad (TOPOgraphic PARAMeter Sonar) system during the expedition HYDRODEC-2000 with R/V *Hespérides* in the austral summer of 2000–2001. This system is a hull-mounted seabed and sub-bottom echosounder based on a parametric acoustic array, which operates using non-linear acoustic properties of the water (Dybedal and Boe, 1994). The system transmitted approximately every 1 s (~10 m at cruise speeds of 10 knots) with a beam angle of approximately 5°, and a modulated frequency sweep (chirp) between 1.5 and 4 kHz. The data were deconvolved and corrected for spherical spreading with a linear time-varying gain prior to presentation. The vertical resolution of the TOPAS records is very high (less than 1 m) and the penetration in this area ranges from a few to several tens of metres. We employed both chirp and ricker-type wavelets, depending on the resolution/penetration rates required. In this way, this system reached resolutions less than 0.5 ms TWT and penetration ranging from 50 to 100 ms TWT, allowing a detailed view of the internal configuration of the seafloor, sub-seafloor and vent conduits.

Multibeam bathymetry of Port Foster was acquired with a Simrad EM1000 (Fig. 2). The EM1000 works at a frequency of 95 kHz, and may be operated in water depths between 3 and 1000 m. In shallow mode, it uses 60 beams spaced at 2.5°, thus covering a sector up to 150° or about 7.5 times the water depth. The beams are 3.3° and 2.4° wide in transverse and forward directions, respectively. The data are positioned using differential GPS. In addition, temperature, conductivity, fluorimetry and sigma-T onboard measurements of the surface waters were registered every 2 min simultaneously with acoustic data.

Table 1
Table of geochemical data for sediment samples obtained in Port Foster, Deception Island

Sample	Fraction	Group	Station	Depth (m)	TiO ₂ (%)	Al ₂ O ₃ (%)	Fe ₂ O ₃ (%)	MgO (%)	CaO (%)	Na ₂ O (%)	K ₂ O (%)	Li (ppm)	P (ppm)	Sc (ppm)	V (ppm)	Cr (ppm)	Mn (ppm)	Co (ppm)	Ni (ppm)	Cu (ppm)	Zn (ppm)	As (ppm)	Rb (ppm)	Sr (ppm)	Y (ppm)	Ba (ppm)	W (ppm)	Pb (ppm)
DT06	bulk	1A	6	134	1.60	14.27	8.59	3.06	5.92	4.86	0.80	12	1881	15	294	29	1221	68	12	35	91	56	5	321	27	140	155	12
DT07	bulk	1A	7	118	1.57	14.06	8.39	2.99	5.74	5.01	0.80	13	1883	14	228	26	1223	46	11	33	86	42	6	322	27	129	140	12
DT16	bulk	1A	16	162	1.70	15.10	9.90	3.29	5.91	5.05	0.91	14	2004	16	192	23	1199	25	10	45	99	25	6	321	28	125	10	16
DF16	clay	1A	16	162	1.68	14.57	9.48	3.26	5.81	4.70	0.89	14	1959	16	192	25	1171	24	12	45	93	31	9	337	28	123	10	13
DT28	bulk	1C	28	110	1.73	15.21	9.81	3.36	6.37	4.98	0.85	14	2054	17	204	25	1132	28	10	46	98	31	4	354	26	117	13	12
DT29	bulk	1B	29	129	1.68	14.95	9.61	3.24	6.13	5.05	0.86	13	2132	16	193	27	1217	26	11	42	98	30	7	348	27	119	11	15
DT32	bulk	1C	32	160	1.72	15.14	9.64	3.29	6.30	4.92	0.84	13	2020	16	201	27	1270	36	10	43	95	25	6	356	26	119	40	11
DF39	clay	1C	39	134	1.70	14.38	9.68	3.31	6.02	4.46	0.83	13	2238	16	208	24	1179	25	11	47	91	33	8	339	27	116	15	11
DT39	bulk	1C	39	134	1.73	14.72	9.75	3.26	6.22	4.86	0.80	13	1982	17	214	20	1182	32	10	49	94	22	6	348	25	114	25	11
DT41	bulk	1B	41	94	1.77	15.33	9.62	3.51	6.55	5.12	0.85	13	1935	18	210	24	1270	29	10	47	96	27	6	361	27	115	32	13
DF41	clay	1B	41	94	1.78	15.06	9.71	3.44	6.33	4.58	0.85	13	1982	17	208	25	1242	28	11	47	93	25	8	341	27	118	29	13
DT44	bulk	1B	44	116	1.72	15.06	9.61	3.39	6.24	5.27	0.88	13	2126	17	200	24	1361	27	10	44	96	26	7	352	27	119	16	13
DF44	clay	1B	44	116	1.72	14.78	9.88	3.36	6.17	4.52	0.85	13	2122	17	202	25	1266	27	12	45	102	25	8	344	28	120	14	13
DD54	sand	2	54	–	1.93	15.48	9.40	3.54	7.14	4.97	0.77	13	1396	18	223	25	1164	41	11	48	92	20	4	364	26	116	158	12
DT55	bulk	1C	55	–	1.82	15.46	10.00	3.02	6.43	4.85	0.80	13	1965	16	181	20	1135	33	10	34	91	76	7	362	28	127	76	13
DD56	sand	2	56	–	1.77	16.07	9.15	4.09	7.91	4.57	0.68	11	1389	20	205	38	1092	32	20	35	84	20	4	399	24	101	81	10
DD69	sand	2	69	–	1.83	15.50	9.37	4.17	7.48	4.58	0.92	10	1234	21	242	31	1103	36	16	59	84	20	4	377	23	93	79	10
DD70	sand	2A	70	–	2.05	16.14	10.10	3.76	7.84	4.90	0.71	12	1345	20	262	24	1203	42	12	63	93	20	4	369	26	113	133	12
DT70	bulk	2A	70	–	1.98	16.39	10.12	3.97	8.05	4.64	0.66	11	1370	21	259	24	1191	44	11	56	95	20	4	385	25	105	123	12
DT71	bulk	2	71	–	1.97	16.18	10.24	3.81	7.63	4.70	0.70	11	1356	19	256	64	1172	64	10	58	94	20	4	370	24	110	198	11
DT73	bulk	1B	73	–	1.92	15.72	10.11	3.06	6.50	5.13	0.85	14	1631	16	215	15	1243	41	10	56	97	20	7	356	29	131	142	13
DD73	sand	2	73	–	1.93	15.59	9.84	3.14	6.58	5.17	0.84	13	1491	16	216	26	1183	42	10	55	93	20	4	351	27	130	148	11
DT74	bulk	2B	74	–	1.95	15.84	10.70	3.72	7.25	4.73	0.74	12	1928	20	233	34	1176	46	13	48	96	20	4	377	26	108	148	14
DT75	bulk	2	75	–	2.03	16.35	10.48	3.92	7.87	4.85	0.71	11	1662	21	252	36	1236	36	12	47	97	21	4	365	27	106	89	12
DD75	sand	2	75	–	1.90	15.69	9.74	3.96	7.85	4.58	0.65	10	1502	22	247	38	1214	38	17	51	94	21	4	365	26	105	95	10
DT76	bulk	1B	76	–	1.75	16.24	9.52	3.12	6.61	5.19	0.91	13	1623	16	180	20	1232	32	10	35	101	20	4	342	31	138	89	13
DD76	sand	2	76	–	1.92	15.37	9.52	3.64	7.34	4.77	0.71	11	1455	19	225	23	1167	35	12	45	93	20	4	355	27	109	87	12
DB77	gravel	2A	77	–	2.14	16.08	10.24	5.64	9.06	4.15	0.52	9	1601	23	250	86	1180	55	48	41	87	20	4	422	24	71	211	10
DB78	gravel	2A	78	–	1.98	16.61	10.12	5.76	9.66	4.13	0.50	8	1366	25	249	88	1170	45	39	33	84	20	4	416	23	69	96	11
DT79	bulk	2	79	–	1.98	16.39	10.35	4.39	8.40	4.50	0.62	10	1448	22	249	41	1216	40	18	47	92	20	4	389	25	95	111	13
DD79	sand	2	79	–	1.95	15.88	9.68	4.36	8.23	4.54	0.64	10	1386	22	242	45	1159	38	20	49	86	20	4	376	25	95	109	11
DT80	bulk	2	80	–	1.97	16.59	10.44	4.36	8.4	4.53	0.65	11	1476	22	248	42	1202	43	19	49	90	20	4	392	23	98	108	11
DD80	sand	2	80	–	1.90	15.63	9.51	4.01	7.64	4.66	0.68	11	1400	20	229	35	1144	37	16	47	87	20	4	376	25	101	108	11
DT81	bulk	2	81	–	1.83	16.18	10.48	4.11	7.91	4.34	0.68	11	1567	20	236	33	1138	45	21	59	93	35	4	380	24	108	91	12
DT82	bulk	2	82	–	1.88	15.74	10.75	3.51	7.11	4.74	0.77	12	1816	18	215	30	1174	75	11	43	94	53	4	353	28	118	251	12
DB82	gravel	1A	82	–	1.25	15.63	7.48	2.40	5.18	5.59	1.10	13	1627	10	92	29	1098	29	11	22	88	30	12	282	35	169	146	12
DB83	gravel	2A	83	–	1.35	16.95	8.09	5.11	9.02	3.91	0.54	13	1066	21	188	86	908	34	43	59	70	20	8	345	18	98	63	11

See Fig. 2A for sample locations.

The geochemical grid used in this paper consisted of 37 sediment samples. Twenty were bulk samples (mixed sand/mud, labelled as DT), four of gravel (DB) and nine of sand (DD) (see Table 1). In addition, four samples were mud-grade splits from bulk samples (DF). The analyses were carried out in the Centro de Laboratorios y Ensayos del IGME de Madrid, Spain. Rb, Sr and Li were analysed by Atomic Absorption Spectrophotometry using a Thermo Jarrell Asf Smith–Hieftje 8000, and major (Al, Ca, Fe, K, Mg, Na, Ti) and trace (Li, As, Ba, Rb, Sr, Co, Cr, Cu, Mn, Ni, P, Pb, Sc, V, W, Y, Zn) elements were determined using a multi-channel Inductively Coupled Plasma–Atomic Emission Spectroscopy (ICP–AES) Thermo Jarell Ash ICAP61. Elemental dissolutions in HCl 10% and the SO-1, SO-2, NBS-2704, and BM reference standards were used for analysis quality control. REE analyses were determined by fusing 0.2-g sample with 1.2 g LiBO₂, dissolved and diluted to 100 ml with 5% HNO₃ and analysed by Inductively Coupled Plasma–Mass Spectrometry.

5. Results

5.1. Ultrahigh-resolution seismic study

A thick volcanic–hydrothermal sedimentary sequence is observed on the medium-resolution seismic lines (Sparker) that run in a SE–NW direction from Neptunes Bellows toward the deeper basin of Port Foster. System penetration of up to 300 ms TWT time (around 120 m at 1530 m/s) allowed us to observe a sequence of deposits bounded by unconformities caused by progressive tilting (Fig. 3, from Rey et al., 1995). The sequence was correlated by Rey et al. (1995) with tectono–volcanic events producing volcanic edifices by magma intrusion and tilting of the underlying deposits based on a stratigraphy by Birkenmajer (1992). However, the recently published more rigorous stratigraphy by Smellie (2001) casts doubt on the basis of several of those correlations (acknowledged by Rey et al., 2002). The uppermost unit of this sequence onlaps a tilted strong unconformity characterised by the presence of

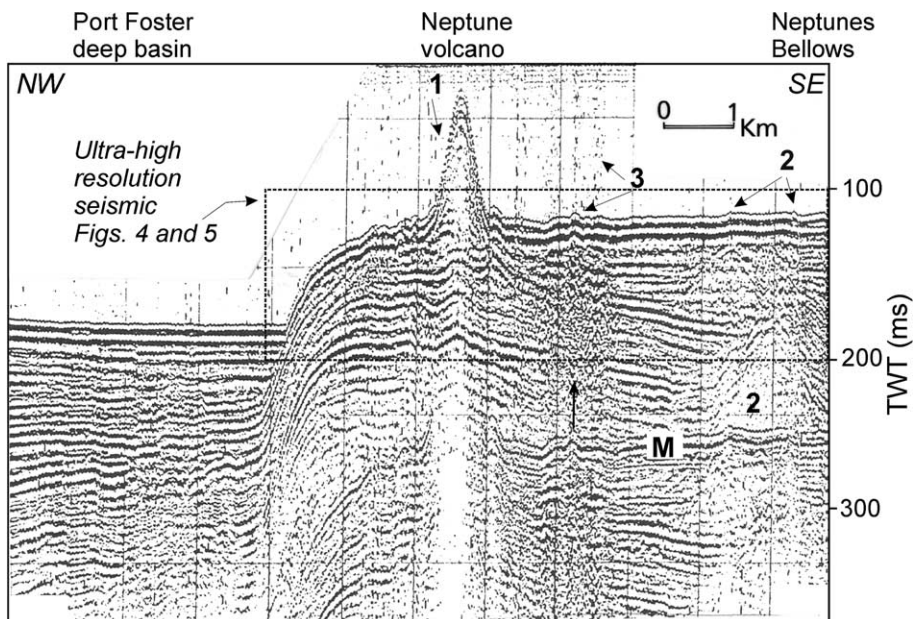


Fig. 3. Medium-resolution seismic profile (sparker) from Port Foster showing: (1) the ‘Neptune submarine volcano’ (Stanley Patch), (2) mound structures, and (3) vents associated with subsurface acoustic masking interpreted as fluid-enriched sediments (arrow). The dashed box on the profile indicates the approximate position of the section covered by the ultrahigh-resolution seismic profile shown in Figs. 4 and 5. See Fig. 2B for location of profile. M indicates location of the seafloor multiple.

chaotic mound-shaped reflectors interbedded with near-parallel reflectors. The layering of the mounds suggests a significant overall thickness of about 40–50 m.

The medium-resolution seismic lines show evidence of three types of volcanic and hydrothermal-related structures within the uppermost seismic unit (Fig. 3): (1) volcanic edifices (cones), (2) mound-like structures, and (3) hydrothermal fluid vents. In some cases, the volcanic cones give rise to prominent landforms on the seafloor with heights of 50 m ('1' in Fig. 3), which are well mapped toward Neptunes Bellows (Fig. 2B). The cones are aligned NW–SE (Fig. 2A). Active fissures are present on the flanks of some of them (Fig. 2D). Mounds occur between Stanley Patch and Neptunes Bellows and are acoustically characterised by chaotic and transparent facies ('2' in Fig. 3). The mounds appear to be linked to normal faults dipping toward the deeper basin of Port Foster. In addition, the presence of subsurface vertical zones of disturbed seismic response characterised by increased amplitudes is interpreted to be due to shallow trapped fluids (liquid/gas; '3' in Fig. 3).

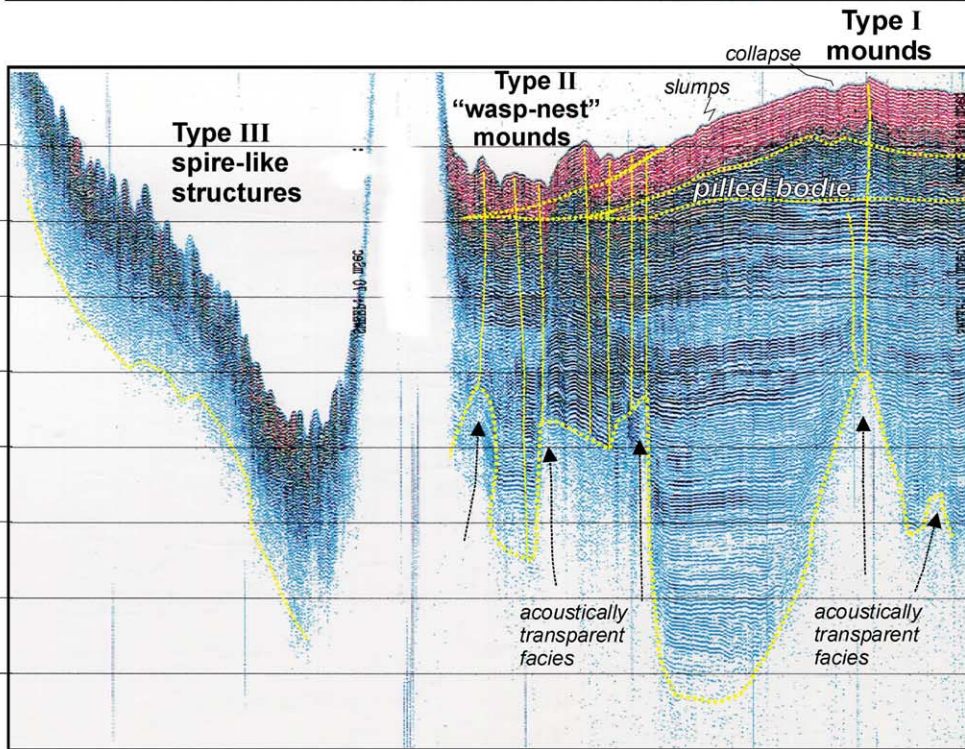
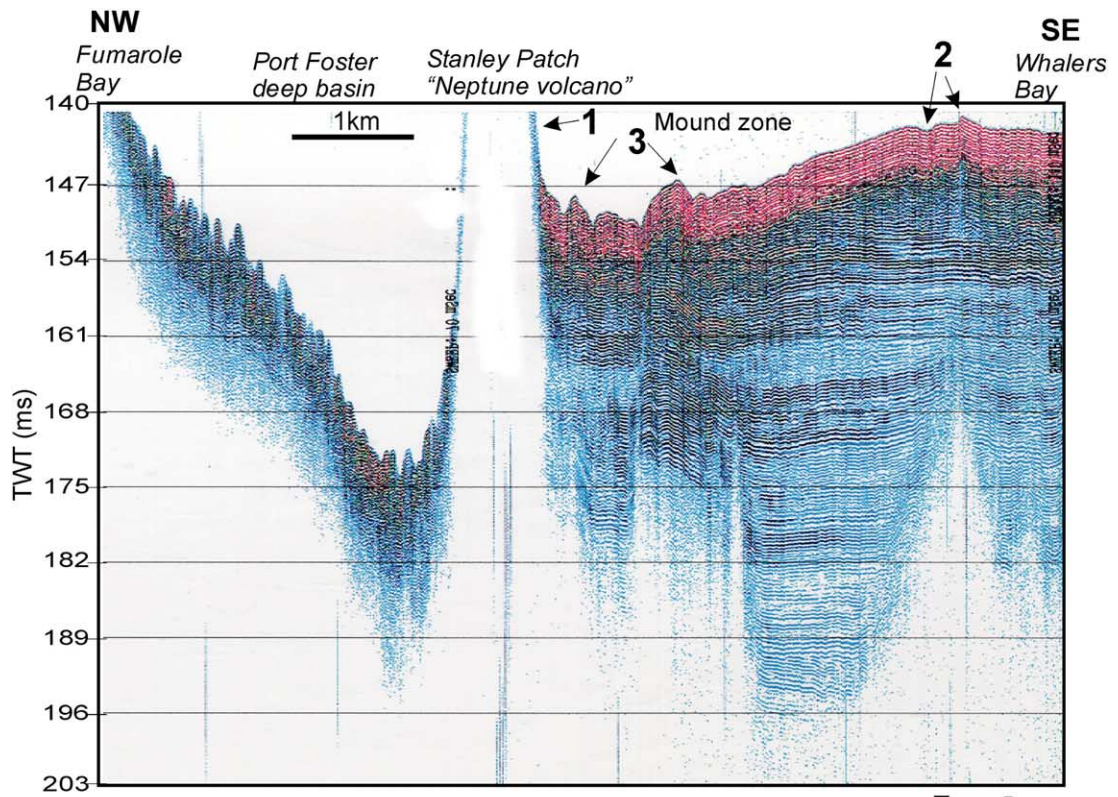
The ultrahigh-resolution seismic lines carried out with the parametric echosounder TOPAS, reveal details of the internal organisation and morphologies of the three types of volcanic and hydrothermal structures mentioned above (Figs. 4 and 5). Each prominent morphology on the seafloor is connected at depth to acoustically transparent dome-like structures by vertical conduits that deform the surrounding stratigraphy. The non-reflective acoustic response in those basal structures is interpreted as evidence for fluid-enriched sediments that have entirely absorbed the acoustic energy. Three types of vent-related mounds are observed in Fig. 4:

Type I, *low-relief mounds* ('2' in Fig. 4), have a convex-up morphology with a conspicuous step-like summit discordance 1 m tall, that marks the position where the central conduit reaches the seafloor. A large sediment apron extends 800–900 m from the crest and reaches a maximum thickness of 17–20 m. The internal structure of the low-relief mounds is composed of oblique reflectors that dip radially out from the presumed axial vent

(conduit), reflecting repeated sediment deposition from radially flowing unconfined currents. The entire mound is polygenetic and comprises two or possibly three superimposed edifices (Figs. 4 and 5). Gravitational collapse and slump structures are present on its top and flanks, respectively. This type of mound is correlated with the uppermost mound-like structures which are poorly observed on the medium-resolution lines ('2' in Fig. 3)

Type II, *high-relief mounds*, which rise 4–5 m above the seafloor, show more prominent crests than the low-relief mounds. At least five high-relief mounds can be observed on the seismic sections (Fig. 5). They show steep asymmetric flanks and rounded crests that rise sharply above the surrounding seafloor and resemble the 'wasp-nest' mound structures described in other hydrothermal fields (Murton et al., 1995; Humphris et al., 1995). Near-vertical flanks are observed on the northernmost mounds. Below the seafloor, seismically distorted vertical columns are linked to acoustically transparent zones at depth ('3' in Fig. 4). These columnar zones are formed by increased amplitude and inverse-phase reflectors typical of seismic anomalies associated with gas 'chimneys' (gas-enriched fluid migration pathways) in fault systems (e.g. Aminzadeh and Conolly, 2002). In addition, this type of vent is correlated with the chaotic zone within stratified sediments observed on the medium-resolution seismic lines ('3' in Fig. 3). Dispersed reflectors observed within the seawater column and just above the summit conduit indicate the presence of buoyant plumes of escaping fluids ('3' in Fig. 3) and an actively discharging vent system.

Type III, *'spire-like' structures*, were only observed in the deeper basin of Port Foster, mainly near Fumarole Bay (Fig. 4). These structures are tall (2–3 m) and narrow, with steep walls, and they do not show any obvious subsurface conduits like the other two vent types. The non-reflective zone just below the spire-like structures might represent the upper surface of the shallow aquifer that also feeds the nearshore fumaroles (e.g. in Fumarole Bay and Pendulum Cove; Fig. 4). Both spire-like structures and the shallow-water fumaroles are associated with NE–SW



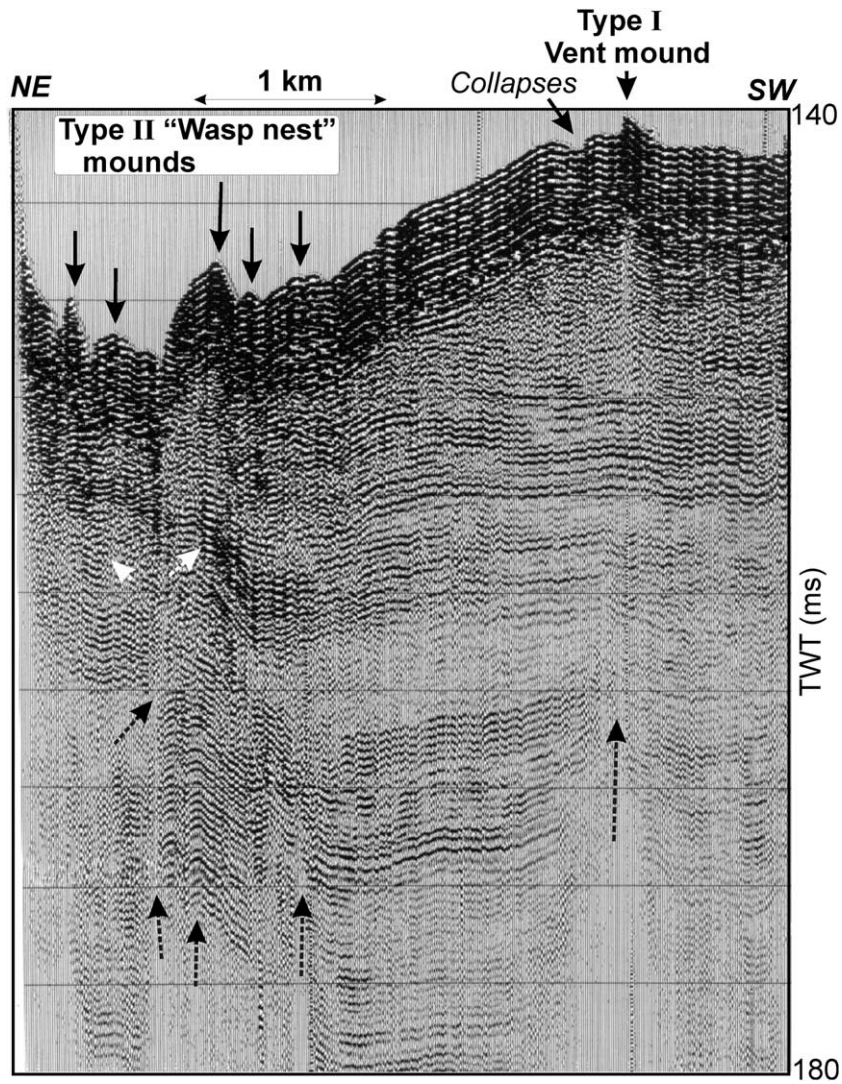


Fig. 5. Ultrahigh-resolution TOPAS profile showing seafloor mounds and vents located southeast of Stanley Patch (‘Neptune submarine volcano’). Note the vertically-stacked shift in polarity defining columnar distorted zones (indicated with white arrows) interpreted as fluid conduits, linked to seafloor mound structures (thick line arrows). Transparent conduits rising from basal transparent zones, interpreted as subsurface aquifers, are also indicated (stippled arrows). See Fig. 2B for location of profiles.

Fig. 4. Ultrahigh-resolution TOPAS profile and interpretation showing vertical distorted zones used by fluids in fractures and fissures in the sediment rising from underlying deep aquifers; the latter are observed as a basal acoustically transparent zone. Numbered labels indicate the same seafloor features as in Fig. 3. Colour indicates reflectivity levels from high (red) to low (light blue). See Fig. 2B for location of profile.

near-vertical fissures crossing the deep basin of Port Foster (Fig. 2A).

5.2. Geochemistry of seafloor sediments

Two main geochemical groups have been detected on the basis of our analytical study of 24 elements in the 26 samples collected in Port Foster. The analyses are presented in Table 1. Based on principal component factor analysis, two main groups are distinguished (Rey et al., 1997). Group 1 is characterised by higher contents of Na₂O, K₂O, P₂O₅, Li, Rb, Ba, Y, and As, and higher Sr/Ca ratios. Within this group, three subgroups are identified (Table 1): one with very low contents of all major elements and with higher concentrations of Cr, Co, and V (group 1a); a second with higher concentrations of Na₂O, K₂O, Y, Pb, and Zn (group 1b); and a third subgroup with characteristics intermediate between the other two subgroups (group 1c). Group 2 is characterised by higher contents of Al₂O₃, Fe₂O₃, MgO, CaO, TiO₂, Sr, Sc, Cr, Ni, Co, Cu, V, and W, and lower Sr/Ca ratios. In Group 2 two subgroups were identified: group 2a, with slightly higher contents of MgO, CaO, and Sr, and group 2b, with higher concentrations of Fe₂O₃, Na₂O, K₂O, TiO₂, P₂O₅, Y and Zn.

All the fine-grained sediments from the deeper parts of Port Foster correspond to Group 1. In major oxide contents, Group 1 has a limited range of relatively evolved compositions, whereas Group 2 is less evolved and has a much wider compositional range than Group 1. There are difficulties in precisely comparing major oxide analyses obtained by different analytical methods (in this case, ICP–AES and X-ray fluorescence), but the compositional relationship between the two sediment groups is similar to that displayed by post-caldera magmas erupted on the island: the 1967–1970 eruptions were all andesitic (cf. Group 1), whereas other post-caldera tephros were less evolved except in rare instances (cf. Group 2; Smellie, 2002b). We thus suggest that the Group 1 sediments were probably deposited in Port Foster as tephra from the 1967–1970 eruptions, whilst the compositionally more heterogeneous and less evolved Group 2 was probably sourced from sev-

eral pre-1967 centres. The distribution of Group 1 is virtually confined to the deeper parts of Port Foster, where the accumulation of fine-grained sediments is probably dominated by slow suspension sedimentation from waning sediment gravity flows sourced in the steep basin-margin slopes (cf. Rey et al., 2002), or by direct input as ashfall tephros from eruptions (cf. tephra distribution from 1967–1970 eruptions; Baker et al., 1975). The sample distribution for Group 1 is encompassed by the area affected by 1967–1970 tephra (Baker et al., 1975), and input as ashfall is plausible. By contrast, Group 2 is restricted to the margins of Port Foster and includes western locations that were outside of the 1967–1970 tephra fall. We suggest that the Group 2 sample sites would have received abundant detritus from numerous sources (presumably including 1967–1970 tephra, but only as one component among many) reworked by surficial streams (López-Martínez and Serrano, 2002). Because Port Foster is an enclosed caldera basin with a shallow sill and narrow entrance, it receives detritus weathered solely from tephros and (much less common) lavas erupted on Deception Island itself. Therefore, the compositions of the Deception Island tephros and lavas can be used with some confidence as a baseline with which the compositions of the Port Foster sediment samples can be compared (cf. Table 1).

5.3. REE patterns

N-MORB normalised REE patterns (see data in Table 2) for the Deception Island sediments display values that clearly fall between average values for E-MORB and OIB for LREE, whereas the HREE values are generally similar or slightly enriched compared to those of N-MORB (Fig. 6). The Deception Island sediments are LREE enriched, with (La/Yb)_N ratios of 4.0–8.2 and (La/Sm)_N ratios of 2.0–4.2. They also have anomalous peaks for Eu, Tb, and Tm compared with subaerial tephros and lavas on the island, which they otherwise closely resemble. The HREE patterns are near-parallel to N-MORB values with (Gd/Yb)_N ratios of 1.2–1.4. The REE patterns (Fig. 6A) are similar to those of hydrothermal waters

Table 2
REE data for sediment samples from Port Foster, Deception Island

Sample	Group	Station	Depth (m)	La (ppm)	Ce (ppm)	Pr (ppm)	Nd (ppm)	Sm (ppm)	Eu (ppm)	Gd (ppm)	Tb (ppm)	Dy (ppm)	Ho (ppm)	Er (ppm)	Tm (ppm)	Yb (ppm)	Lu (ppm)
DT06	1A	6	134	12.8	39.6	4.5	22.4	5.4	3.7	5.4	1	5.7	1.8	3.7	0.5	3.4	0.5
DT07	1A	7	118	11.7	33.9	2.9	20.7	4.5	1.8	5.3	0.2	5.5	1.9	3.0	0.5	3.4	0.6
DT16	1A	16	162	11.0	50.5	2.9	21.2	4.9	1.8	5.4	0.2	5.9	1.6	3.3	0.5	3.4	0.5
DF16	1A	16	162	14.1	46.4	4.2	28.9	5.4	4.1	6.3	0.7	5.9	1.2	4.1	1.1	4.2	0.8
DT28	1C	28	110	13.2	38.9	4.1	22.4	5.8	2.0	5.8	0.7	6.0	1.5	3.8	1.1	3.7	0.5
DT29	1B	29	129	12.2	43.7	4.1	21.5	5.5	2.0	5.8	1.1	5.7	0.9	3.5	0.5	3.6	0.5
DT32	1C	32	160	13.7	39.6	4.4	22.5	5.5	2.0	5.9	1.0	5.6	2.2	3.6	0.5	3.7	0.5
DT39	1C	39	134	12.8	38.2	3.9	22.6	5.7	2.1	5.9	0.6	6.1	1.7	3.7	0.9	3.8	0.5
DF39	1C	39	134	13.9	39.4	4.5	26.7	6.0	2.1	6.4	0.8	5.9	1.5	3.3	1.3	4.2	0.5
DT41	1B	41	94	11.9	41.1	2.8	22.0	4.9	2.0	5.9	0.2	5.9	1.9	3.2	0.5	3.6	0.5
DF41	1B	41	94	21.6	33.6	3.8	23.1	4.7	1.8	5.7	0.5	5.6	1.1	3.2	1.5	3.7	0.7
DT44	1B	44	116	23.3	50.8	4.1	24.4	6.3	2.7	6.4	0.3	6.8	2.1	4.4	0.5	4.2	0.8
DF44	1B	44	116	11.1	31.2	3.1	21.7	4.6	1.7	5.3	0.6	5.4	1.5	3.1	1.6	3.5	0.5
DD54	2	54	–	15.1	41.7	3.8	23.1	5.4	2.0	5.7	0.3	6.3	1.3	3.5	0.5	3.8	1.1
DT55	1C	55	–	15.1	43.3	3.6	24.3	5.4	2.2	6.2	0.6	6.0	1.6	3.6	0.6	4.0	0.5
DD56	2	56	–	22.0	49.6	4.2	23.1	6.0	2.6	6.0	1.4	6.0	1.6	3.8	1.8	3.9	1.4
DD69	2	69	–	11.5	35.1	3.1	19.7	5.1	2.0	5.2	0.3	5.2	2.1	3.2	0.5	3.2	0.5
DD70	2A	70	–	12.2	37.1	3.3	20.7	4.8	1.9	5.6	0.2	5.6	1.6	3.0	1.0	3.4	0.6
DT70	2A	70	–	10.2	33.6	2.3	20.0	4.4	1.9	5.4	0.2	5.5	1.5	3.4	0.5	3.3	0.5
DT73	1B	73	–	16.7	44.5	3.5	24.9	5.2	2.2	6.3	0.2	5.9	1.7	3.9	0.5	4.1	0.5
DD73	2	73	–	15.2	47.0	3.6	25.6	5.4	2.3	6.4	0.2	6.7	2.0	4.1	0.5	4.2	0.8
DT74	2B	74	–	11.3	37.9	3.2	22.0	4.9	2.0	5.7	0.2	5.7	1.8	3.3	0.5	3.6	0.5
DT75	2	75	–	12.6	39.6	4.5	23.3	6.4	2.2	6.2	0.9	5.4	1.7	3.4	0.7	3.8	0.6
DD75	2	75	–	11.3	37.7	3.3	21.0	5.2	2.0	5.6	0.7	5.7	1.9	3.3	0.5	3.4	0.5
DT76	1B	76	–	19.4	55.3	5.7	29.5	7.2	2.4	7.4	0.8	7.1	1.8	4.9	1.6	4.9	1.2
DD76	2	76	–	15.6	44.7	4.2	24.1	5.6	2.0	6.1	0.6	6.0	2.1	3.9	0.5	4.1	1.1
DB77	2A	77	–	15.5	33.6	2.8	19.2	4.2	1.8	5.1	0.2	4.8	1.8	2.9	0.5	3.0	0.8
DB78	2A	78	–	11.1	31.2	2.6	18.1	4.0	1.8	4.8	0.2	5.2	1.4	3.3	0.5	3.0	0.9
DD79	2	79	–	13.0	37.0	3.2	20.5	4.3	1.9	5.5	0.4	5.6	2.0	3.0	0.5	3.4	1.1
DT80	2	80	–	11.8	34.1	3.8	19.8	4.5	1.9	5.5	0.2	5.0	1.5	3.4	0.5	3.2	0.7
DD80	2	80	–	11.9	36.8	3.2	20.1	4.8	2.0	5.4	0.5	5.7	1.3	3.5	0.5	3.3	1.1
DT81	2	81	–	14.6	36.2	3.5	20.6	4.7	1.9	5.6	0.3	5.6	1.7	3.4	0.5	3.4	0.5
DT82	2	82	–	14.1	41.2	3.9	22.8	5.5	2.1	5.7	0.7	5.7	1.4	3.5	0.5	3.8	0.7
DB82	1A	82	–	17.8	54.0	4.7	27.0	6.6	2.1	6.6	0.2	7.0	2.0	4.3	1.0	4.5	1.3
DB83	2A	83	–	16.2	28.8	2.6	16.2	4.3	1.5	3.9	0.7	4.2	0.7	2.3	0.9	2.4	1.1

See Fig. 2A for sample locations.

from high-temperature vents. The latter are characterised by LREE-enrichment, and they usually display strikingly positive Eu anomalies relative to N-MORB (Klinkhammer et al., 1994). The REE/NASC pattern is similar to those of hydrothermal deposits from the average EPR 39°S ridge crest sediments (Piper and Graef, 1974) and hydrothermal crusts from the TAG area (Humphris et al., 1995), except that the Deception Island sediments do not have negative Ce anomalies (Fig. 6B).

Group 1 sediments show greater concentrations in Eu (2 samples) and Tm (most samples, especially clay-fractions) than those of Group 2 (Fig. 6A; Table 2). Several Group 2 samples have unusually low Tb values but the range of concentrations between the two groups is very similar. However, the measured concentrations of both Tm and Tb are close to their detection limit by

ICP–AES and the significance of the values we measured is uncertain. The contoured map for La/Sm ratios demonstrates that LREE are significantly enriched (La/Sm_N ratios >4) in sediment samples from the mounds near Stanley Patch in comparison with other parts of Port Foster (La/Sm_N ratios <2; Fig. 7).

6. Discussion

6.1. Seeps and sediment volcanism after magmatic intrusions

Svensen et al. (2002) proposed a new model for seeps and sediment volcanism associated with hydrothermal systems within volcanic basins in the fossil record. The model presented shows several

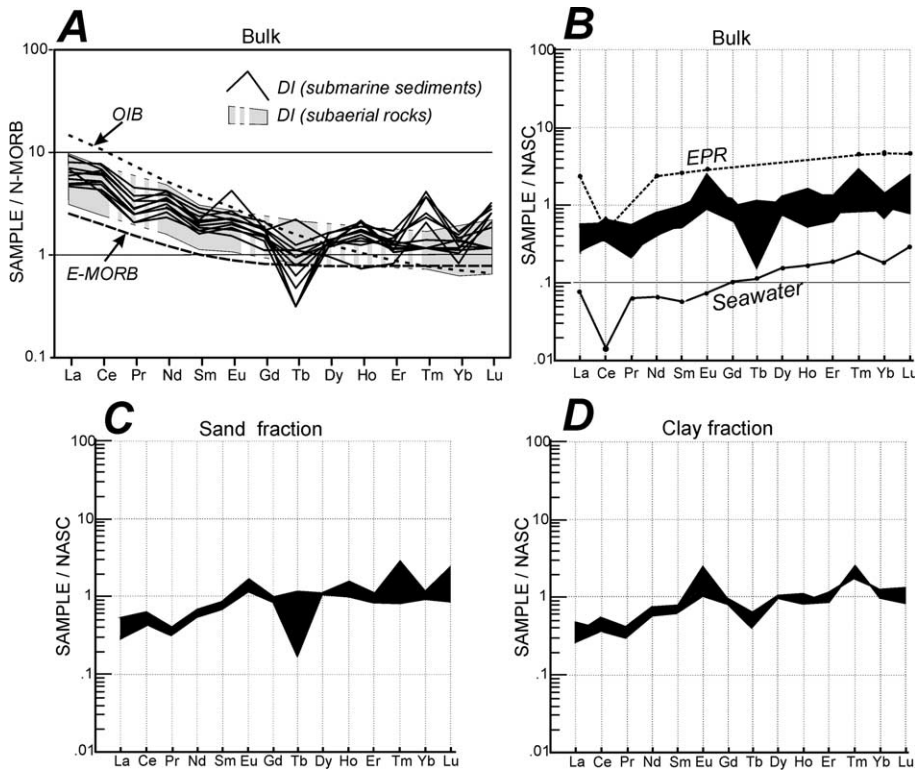


Fig. 6. REE patterns of Deception Island submarine sediments. (A) REE patterns normalised to N-MORB. The range of compositions for late post-caldera-age subaerial eruptions is included for comparison (unpublished data of J.L.S.). (B), (C) and (D) show REE patterns normalised to NASC for bulk sample, sand and clay fractions, respectively, compared with sediments from the 39°S East Pacific Ridge (EPR) hydrothermal field and seawater (data from Piper and Graef, 1974; Klinkhammer et al., 1983). Note that the linear trend for EPR is similar to the pattern for Deception Island. However, a negative Ce anomaly, clearly observed in seawater samples from hydrothermal fields, is not present in Deception Island. The most significant difference with the other patterns is that in all fractions, the trend for Deception Island is punctuated by a sequence of positive anomalies (Ce, Eu and Tm) and a prominent negative anomaly for Tb. See text for explanation.

stages occurred after magmatic intrusions were emplaced in a volcanic sedimentary basin: (1) heating and boiling of pore-fluids caused by intrusion of magma forming a hydrofracture system by increased fluid pressure focused at the tip of the intrusion; (2) explosive hydrothermal eruption generated by fluid decompression, resulting in a hydrothermal complex, brecciation and sediment fluidisation; (3) fluidisation along discrete channels forming pipes and sediment volcanism; and (4) venting of the hydrothermal fracture system re-used as fluid migration pathways, resulting in sites of seep activity.

Ultrahigh-resolution reflection seismic records for Deception Island show three different types of seafloor structures interpreted as edifices vent-

ing fluids at the seafloor: low-relief mounds (Type I), high-relief ‘wasp nest-like’ mounds (Type II) and ‘spire-like’ structures (Type III). Following the model proposed by Svensen et al. (2002), we interpret these structures as products of sediment volcanism and seeps caused by heating and boiling of pore fluids in gas-charged sediments. The compositional resemblance of the Group 1 samples to andesites similar to tephra erupted between 1967 and 1970 suggests that the structures may have formed, or were reactivated, during those eruptions. Additional evidence supporting a very young age includes: (1) the structures crop out on the present seafloor and look essentially unmodified; (2) fumaroles are also active in several areas around the shores of Port Foster

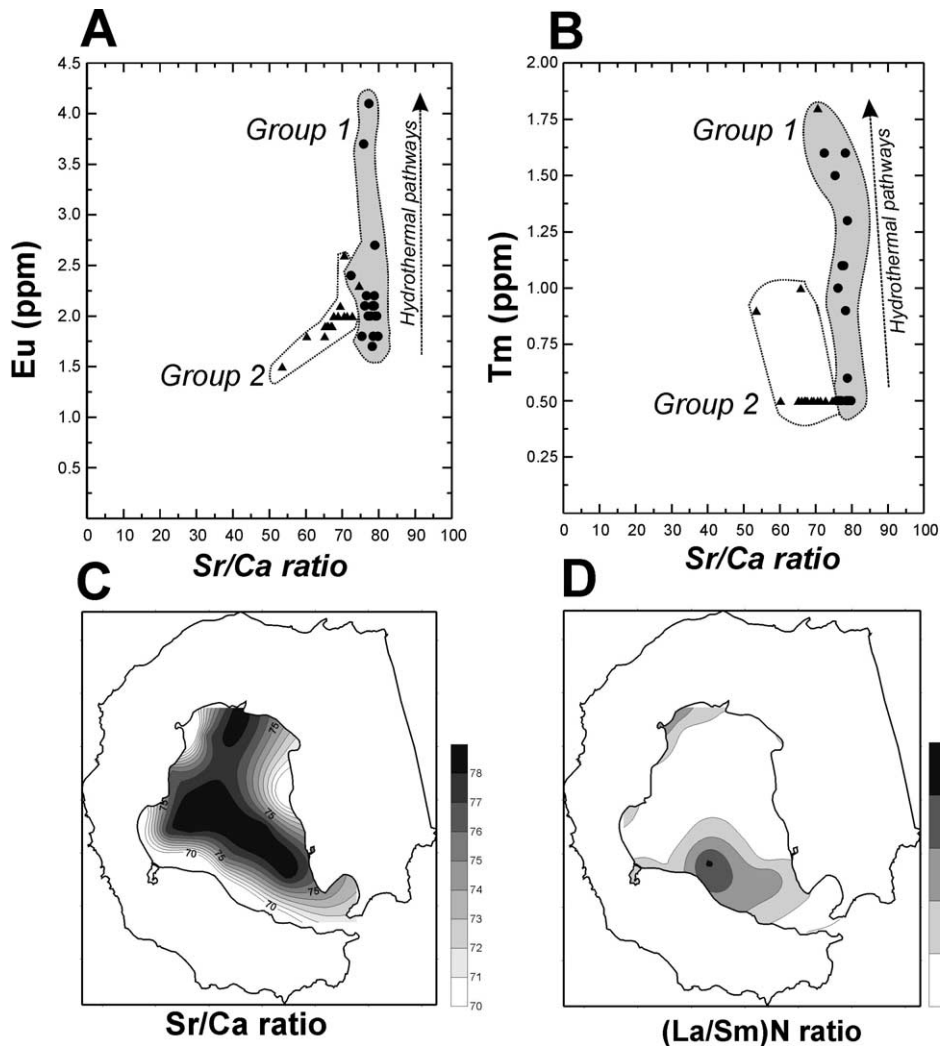


Fig. 7. (A) and (B) show Eu and Tm (ppm) plotted against Sr/Ca, yielding very different Sr/Ca ratios associated with the two sediment groups, two Group 1 samples with very high Eu, and the generally much higher Tm abundances in Group 1 compared with Group 2. (C) Contoured map of Sr/Ca ratios. The ratio may be a proxy for the extent of hydrothermal alteration (and Ca leaching by fluids) in the submarine sediments (see text for explanation). (D) Contoured map of normalised La/Sm ratios showing the distinct enrichment in LREE in samples from the mound deposits shown in Figs. 4 and 5.

and active vents should be anticipated within Port Foster too; and (3) our detection of dispersed seismic reflectors within the water column at one site, at least, indicating fluids escaping in a buoyant plume. This is also supported by the fact that the alignment of the mounds and submarine volcanic cones is NW–SE, parallel and close to the axis of a minimum magnetic anomaly with a more than 3000-nT decrease in field reported beneath

Port Foster and interpreted as linear magmatic intrusion (Garcia et al., 1989). We speculate that the high-relief mounds (Type II), situated NW of the submarine volcano cone (Stanley Patch or ‘Neptune submarine volcano’; Fig. 2), might have experienced explosive hydrothermal eruptions, whereas the low-relief mounds to the SE closely resemble sediment volcanoes formed as a result of subsurface sediment fluidisation, mobili-

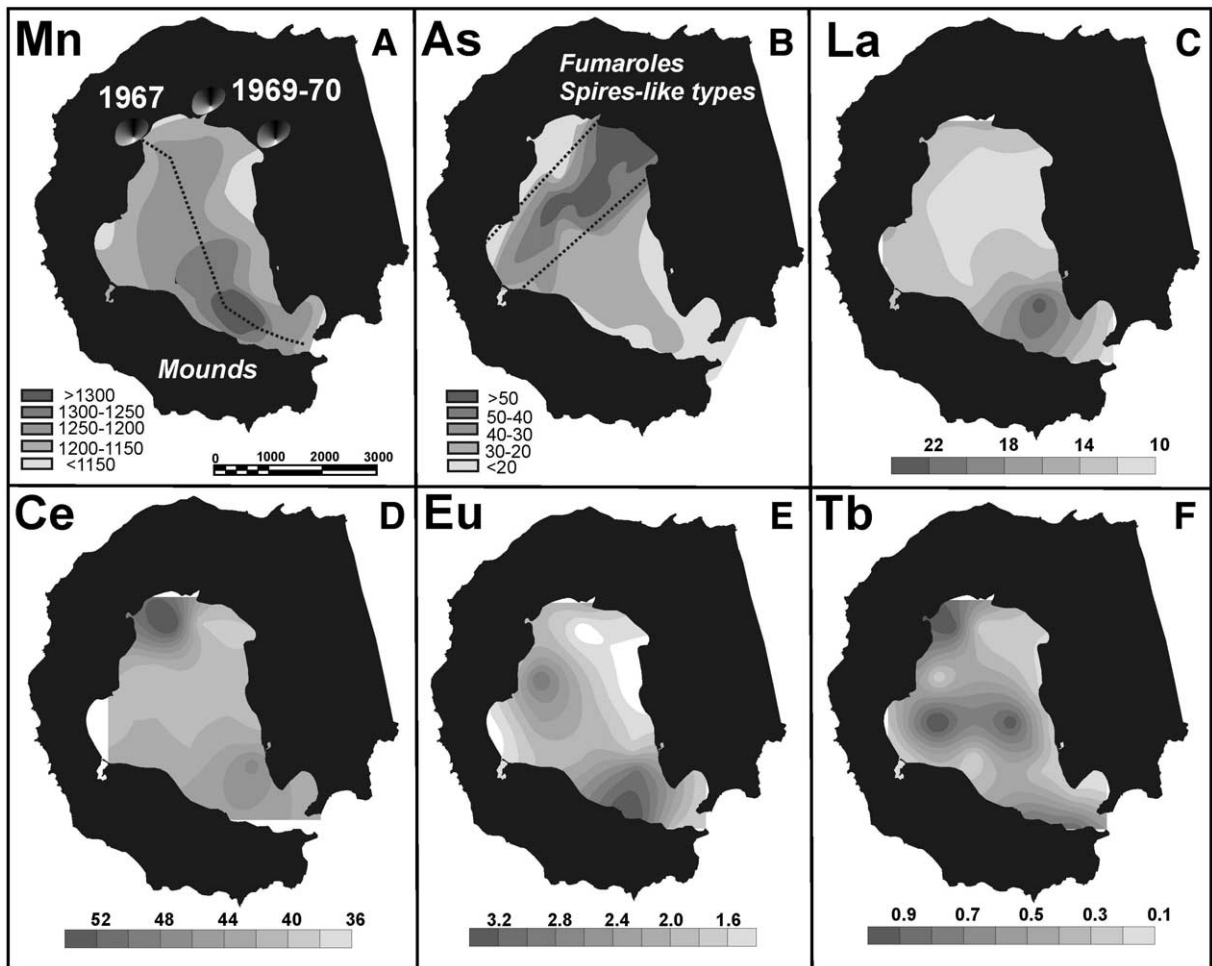


Fig. 8. Contoured maps of Mn, As, La, Ce, Eu, and Tb contents in submarine sediments of Deception Island. Plot contouring in ppm. Trends in geochemical haloes are indicated as stippled lines. Note that the highest contents in Mn show a clear NW–SE trend related to both subaerial volcanic cones and submarine edifices. Otherwise, the highest contents in As coincide with a NE–SW system of faults associated with fumaroles and shallow-water hot springs in Fumarole Bay and Pendulum Cove (see Fig. 2A for location). In addition, La, Ce and Eu show enriched concentrations that correlate with the location of mounds observed on high-resolution seismic profiles (see Figs. 4 and 5).

sation to the surface and radial dispersal from unconfined sediment gravity flows.

Finally, we also suggest that the subsurface ‘acoustic chimneys’ observed in the ultrahigh-resolution seismic profiles are fracture-related hydrothermal conduits that were exploited by fluidised and brecciated sediments. The presence of superimposed mounds suggests that conduits were probably re-used as fluid migration pathways. At least some, possibly many, are still active and were responsible for the seep anomalies and

geochemical haloes which we have detected (cf. Planke et al., 2002).

6.2. Geochemical distribution and seafloor hydrothermal activity

Seafloor sediments in Port Foster vary in their chemical composition. The geochemical halo-like distribution patterns of some elements are interpreted to be caused by seafloor hydrothermal vent activity (Fig. 8). For example, the highest values

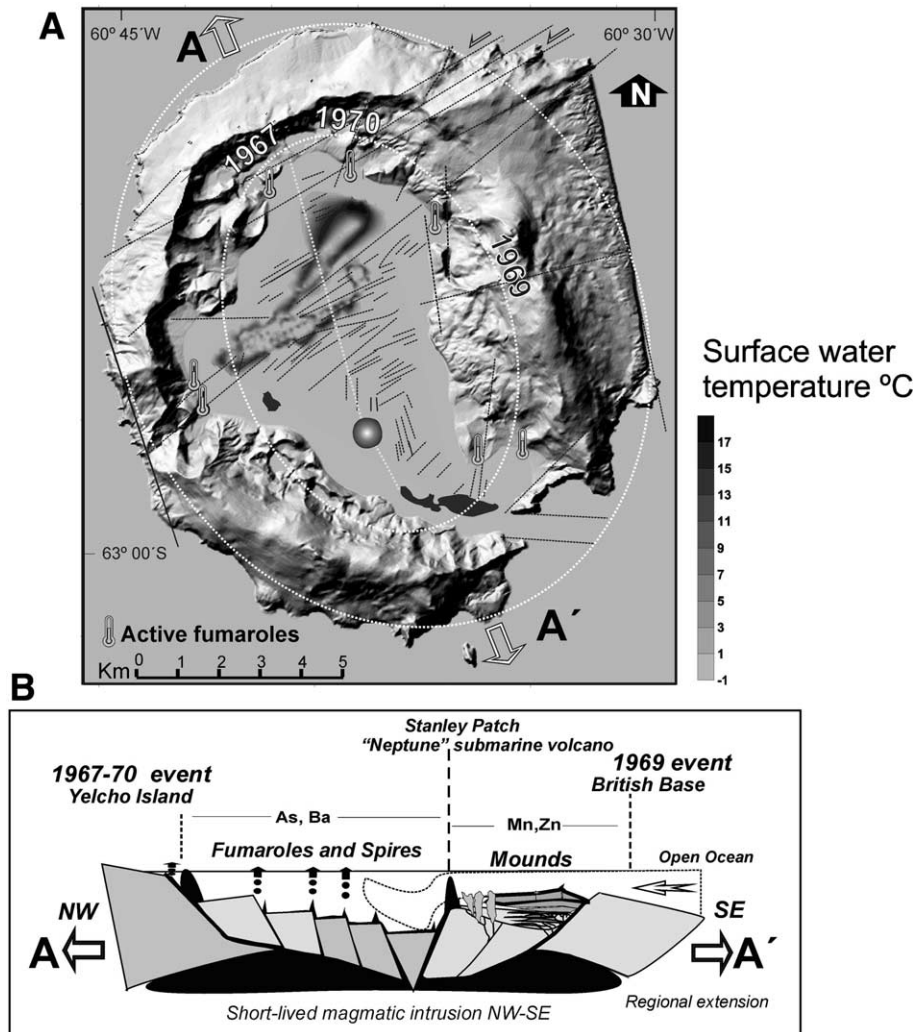


Fig. 9. Schematic model used to explain the relationship between activity of submarine hydrothermal vents, recent volcanic eruptions and fault-related fluid pathways. (A) Theoretical stress ellipsoid projected onto a shaded relief map of Deception Island (dashed white line), showing the relationship between surface water anomalies and normal faults orthogonal to the major axis of the strain ellipsoid. Note that expression of subaerial faults is indicative and based on topography. The alignment of submarine volcanic cones, mounds and the 1967 and 1970 pyroclastic cones, are parallel to the major axis of the strain ellipsoid. Note that the subaerial expression of faults are indicative only and are based on interpretation of topography. See text for explanation. (B) Schematic NE–SW cross-section summarising the relationship between vent types, geochemical patterns, volcanic seafloor structures and extensional faults. The existence of an extensive magma chamber underplating the caldera, and unifying all of the surficial features, is conjectural but is based on the geophysical identification of a linear magmatic intrusion on the northeast side of Port Foster (Garcia et al., 1989). The shaded depiction of surface water temperature distribution is based on data obtained in December 2000 during the HYDRODEC-2000 cruise. See text for explanation.

of Mn and Zn (e.g. Mn > 1360 ppm) are found in deep seafloor sediments of Group 1 clustered around mound and vent structures observed on high-resolution seismic lines described above (Figs. 4 and 5). When extrapolated to the sites

of the 1967 eruption at Telefon Bay, the seafloor structures are NW–SE aligned (Fig. 8A).

Otherwise, the highest values of As, Rb and Ba, (e.g. As > 50 ppm; Ba > 140 ppm) are found between Fumarole Bay and Pendulum Cove, in

Group 1 samples obtained on the deep seafloor of Port Foster. Contoured element concentrations show a clear SW–NE alignment extending between Pendulum Cove and Fumarole Bay (Fig. 8B). At present, active fumaroles (Fig. 9) release vapour consisting of H₂, dissolved methane (CH₄), He and water vapour (Valentin et al., 1989). Sediments from the submarine spire-like structures (Type III) and shallow-water fumaroles contain elevated As–Ba concentrations. That vapour-phase activity is still occurring at the vents, using NE–SW-orientated submarine faults and fissures as conduits (Fig. 9), is also supported by the common occurrence of low-frequency volcanic tremors interpreted to be a consequence of rising hydrothermal fluids (Vila et al., 1992; Felpeto et al., 1995).

6.3. REE patterns and hydrothermal alteration

The sediments of the submarine mounds show enrichment in LREE (normalised to N-MORB). Some samples have slight positive anomalies for Eu and possibly Tm, and possible depletion in Tb compared with fresh Deception Island tephras from the 1967, 1969 and 1970 eruptions (Fig. 6A). Although there are uncertainties in accepting the measured Tb and Tm values, and Eu anomalies are as yet uncommon in Deception Island samples, we suggest that the REE patterns have been affected by submarine hydrothermal alteration since the 1967–1970 eruptions. Specifically, positive Eu anomalies are unusual and generally regarded as an indication of effects of high-temperature hydrothermal solutions (Morgan and Wandless, 1980; Butterfield et al., 1990; Cocherie et al., 1994). They have also been found, for example, in metalliferous sediments from hydrothermal mounds near the Galapagos rift (Corliss et al., 1978) and in the Red Sea (Courtois and Treuil, 1977). The fact that Eu and Tm anomalies are particularly prominent in the clay fraction in the Deception Island samples (Fig. 6D) seems to indicate that the REE mobility is preferentially affecting the fine-grained seafloor sediments more than the coarse fraction. An explanation for these anomalies in hydrothermal systems is that the REE are efficiently removed from solu-

tion by co-precipitation with Fe when hydrothermal fluids mix with seawater. The Eu anomaly can be explained by progressive oxidisation of Eu in fluids above the vents and selective precipitation as a colloidal suspension with Fe (Klinkhammer et al., 1983).

The well-defined differences in Sr/Ca ratios between the two sediment groups (Fig. 7A,B) may be a result of differential Ca loss (greater in Group 1 than in Group 2) compared to Sr during alteration of original plagioclase to hydrothermal plagioclase, as has been reported in other hydrothermal fields (Klinkhammer et al., 1995; Fang et al., 1999). A link to hydrothermal processes for this alteration is supported by the observation that Ca/Mg molar ratios in Port Foster seawater are 5–100 times higher (signifying enhanced Ca uptake by the seawater) during periods of anomalously high seawater temperatures (7–15°C) than in other ('normal') periods (Dykes et al., 2001). Tb and Tm anomalies comparable to those we report here (Figs. 6 and 8) have not been identified elsewhere in the literature. However, until element detection limits are improved for Tb and Tm, our report of those 'anomalies' at Deception Island remains tentative and further studies will be required to identify specific physico-chemical properties of Tb and Tm that could enable such anomalies to develop.

7. Conclusions

This paper presents medium- and ultrahigh-resolution seismic profiles and geochemical data for submarine hydrothermal vents and mounds associated with recent volcanic activity in Port Foster, in the submerged caldera of Deception Island (Bransfield Strait, Antarctica). Our work suggests that caldera-related eruptive and volcano-tectonic processes were critical in determining the occurrence and spatial and temporal evolution of the hydrothermal structures. We propose that these structures are related to sediment volcanism and seeps caused by heating and boiling of pore fluids in gas-charged sediments, probably associated with the recent volcanic events on the island. We also suggest that fluidised and brecciated sedi-

Table 3
Summary of geophysical and geochemical characteristics of seafloor hydrothermal vents at Deception Island

	Type I Mound-type	Type II 'Wasp-nest' mounds	Type III Spire-like structures
Seafloor morphology	Low-relief, 1-m tall asymmetrical chimneys; Sediment apron extends a further 800–900 m	High-relief, asymmetrical step-walls, 4–5-m tall chimneys.	Symmetrical steep walls, 2–3 m
Seismic configuration	Parallel dipping reflectors formed by deposits prograding out from axial vent conduit	Highly reflective reflectors around axial vent conduit	Not observed
Architecture	Two to three mounds superimposed by vent migration; form a 17–20-m tall mound-complex	Vertical aggradation of deposits in cone-shaped mound around an axial conduit	Not observed
Fault patterns	Near-vertical antithetic fissures related to low-angle NW dipping normal faults; NW–SE alignment	Antithetic fissures related to volcanic intrusions; NW–SE alignment	Orthogonal near-vertical fissures associated with tensional NE–SW faults
Geochemical haloes	Mn–Zn enriched	Mn–Zn enriched	As–Ba enriched; slight enrichment in Rb.
REE patterns	Ce–Eu–Tm enriched, High Sr/Ca ratios	Ce–Eu–Tm enriched, High Sr/Ca ratios	Tb–Pr enriched
Interpretation	Subsurface sediment fluidisation along discrete channels forming sediment volcanism. Rising buoyant plumes discharged after recent volcanic eruptions	Explosive hydrothermal eruptions. Dense brine-type fluids discharged after recent volcanic eruptions	Low-salinity, vapour-rich fluids. Closely related to active subaerial fumarole emissions (CO ₂ , H ₂ S, CH ₄ , N ₂)

ments, rising from deep within the caldera sediment pile, formed the pipe-like anomalies observed as acoustic chimneys in the seismic profiles. Table 3 summarises the relationships between geophysical and geochemical characteristics of the seafloor hydrothermal structures. The structures we have identified at Deception Island differ from gas seeps and sediment volcanoes in non-hydrothermal areas (related to gas overpressures in gas-charged sediments caused by e.g. organic matter maturation). They are also different from hydrothermal vent systems found at mid-ocean ridges (formed by seawater impacting magma chambers and lacking sediment volcanoes). Formation of the sediment volcanoes and mounds at Deception Island is thought to be related to hydrofracturing and fluidisation by overpressured fluids (probably mainly seawater) driven by high sub-seafloor temperatures following recent volcanic events. Thus, they may correspond to the type of sediment-dominated hydrothermal vent complexes in volcanic sedimentary basins proposed by Svensen et al. (2002) from the fossil record.

Our results also indicate that an inter-linked fracture network formed by extensional processes can create the subsurface pathways necessary to support seawater convection, and may provide the preferential pathways for fluids to migrate to the surface (Fig. 9). Our data emphasise the role of vent complex formation and permeable pathways for secondary fluid migration in a volcanic basin after magmatic events. In this case, those events may have been the short-lived but spectacular eruptions between 1967 and 1970, but there may also be a genetic relationship with resurgence-related volcano–tectonism associated with a high-level magmatic intrusion detected geophysically within caldera, which has been taking place since the mid-twentieth century, at least. The presence of active hydrothermal systems is supported by the existence of thermal anomalies in surface waters of 7–15°C detected in November 2000 (Dykes et al., 2001) and of 15–17°C in December 2000 during the HYDRODEC-2000 cruise (Fig. 9). The thermal variations suggest that there are seasonal differences in the influence of hydrothermal activity on the temperature and, probably

therefore, the chemical composition of hydrothermal vents at Deception Island.

Acknowledgements

This paper is dedicated to the memory of Jesús Baraza. The research was supported by the Project 'Hidrotermalismo submarino en la Isla de Decepción' (ref. ANT1998-1557-E/HESP) administered by the Spanish Programme for Antarctic Research. We are very grateful for the hard work put in by the Masters, officers and crew of the R/V *Las Palmas* and the R/V *Hespérides* on the various research cruises to collect the data used in this study. We are also grateful to the HYDRODEC-2000 scientific party, to Pablo Rodríguez and the UGBO team for their invaluable assistance with the data collection, and to Santiago del Barrio for his help with the ICP–AES analyses. We also thank Joan Gardner for her comments and assistance with English grammar in an early draft. P. Stoffers and an anonymous reviewer provided thorough constructive reviews that significantly improved the manuscript.

References

- Aminzadeh, F., Conolly, D., 2002. Looking for gas chimneys and faults. *AAPG Explorer*, December, pp. 20–21.
- Baker, E.T., 1995. Characteristics of hydrothermal discharge following a magmatic intrusion. In: Parson, L.M., Walker, C.L., Dixon, D.R. (Eds.), *Hydrothermal Vents and Processes*. Geological Society London, Special Publication 87, pp. 65–76.
- Baker, P.E., McReath, I., 1971. 1970 volcanic eruption at Deception Island. *Nature* 231, 5–9.
- Baker, P.E., McReath, I., Harvey, M.R., Roobol, M.J., Davies, T.G., 1975. The geology of the South Shetland Islands, V. The volcanic evolution of Deception Island. *Br. Antarct. Surv. Sci. Rep.* 78, 1–81.
- Barker, D.H.N., Austin, J.A., Jr., 1994. Crustal diapirism in Bransfield Strait, West Antarctica evidence for distributed extension in marginal basin formation. *Geology* 22, 657–660.
- Barker, P.F., 1982. Cenozoic subduction history of the Pacific margin of the Antarctic Peninsula: Ridge crest–trench interactions. *J. Geol. Soc. Lond.* 139, 787–801.
- BAS, 1985. Tectonic Map of the Scotia Arc 1:3 000 000. BAS (MISC) 3, British Antarctic Survey, Cambridge.
- Birkenmajer, K., 1992. Volcanic succession at Deception Island, West Antarctica: A revised lithostratigraphic standard. *Studia Geol. Pol.* 101, 27–82.
- Butterfield, D.A., Massoth, G.J., McDuff, R.E., Lupton, J.E., Lilley, M.D., 1990. Geochemistry of hydrothermal fluids from axial Seamount Hydrothermal Emissions vent field, Juan de Fuca Ridge: Subseafloor boiling and subsequent fluid–rock interaction. *J. Geophys. Res.* 95, 12895–12921.
- Butterfield, D.A., Massoth, G.J., 1994. Geochemistry of North Cleft segment vent fluids: Temporal changes in chlorinity and their possible relation to recent volcanism. *J. Geophys. Res.* 99, 4951–4968.
- Butterfield, D.A., McDuff, R.E., Mottl, M.J., Lilley, M.D., Lupton, J.E., Massoth, G.J., 1994. Gradients in the composition of hydrothermal fluids from the Endeavour segment vent field: Phase separation and brine loss. *J. Geophys. Res.* 99, 9561–9583.
- Butterfield, D.A., Jonasson, I.R., Massoth, G.J., Feely, R.A., Roe, K.K., Embley, R.E., Holden, J.F., McDuff, R.E., Lilley, M.D., Delaney, J.R., 1997. Seafloor eruptions and evolution of hydrothermal fluid chemistry. *Philos. Trans. R. Soc. Lond. A* 355, 369–386.
- Cocherie, A., Calvez, Y., Oudindunlp, E., 1994. Hydrothermal activity as recorded by Red Sea sediments: Sr–Nd isotopes and REE signatures. *Mar. Geol.* 118, 291–302.
- Cooper, A.P.R., Smellie, J.L., Maylin, J., 1998. Evidence for shallowing and uplift for bathymetric records of Deception Island. *Antarct. Sci.* 10, 455–561.
- Corliss, J.B., Lyle, M., Dymond, D.J., Crane, M., 1978. The chemistry of hydrothermal mounds near the Galapagos rift. *Earth Planet. Sci. Lett.* 40, 12–24.
- Courtois, C., Treuil, M., 1977. Distribution des terres rares et de quelques éléments en trace dans les sédiments récents des fosses de la Mer Rouge. *Chem. Geol.* 20, 57–72.
- Dählmann, A., Wallmann, K., Sahling, H., Sarthou, G., Borhmann, G., Petersen, S., Chin, C.S., Klinkhammer, G.P., 2001. Hot vents in an ice-cold ocean: Indications for phase separation at the southernmost area of hydrothermal activity, Bransfield Strait, Antarctica. *Earth Planet. Sci. Lett.* 193, 381–394.
- Dybedal, J., Boe, R., 1994. Ultra-high resolution sub-bottom profiling for detection of thin layers and objects. *Oceans'94*, Osates, Brest.
- Dykes, K., Sturz, A., Gray, S.C., 2001. Investigation of hydrothermal activity at Deception Island, Antarctica. *GSA Annual Meeting*, Abstract 26270.
- Fang, J.N., Chen, Y.L., Yu, T., Lin, I.C., 1999. The preliminary study of hydrothermal alteration of andesite at Tayukeng, Taiwan. *J. Natl. Taiwan Mus.* 52, 103–111.
- Felpeto, A., Blanco, I., Del Rey, R., Morales, J., 1995. Estudio de eventos de baja frecuencia registrados en Isla Decepción. *Final Proc. V Simposio Estudios Antárticos*, Madrid, pp. 147–154.
- Galindo-Zaldívar, J., Jabaloy, A., Maldonado, A., Sanz de Galdeano, C., 1996. Continental fragmentation along the South Scotia Ridge transcurrent plate boundary (NE Antarctic Peninsula). *Tectonophysics* 259, 275–301.

- Gallardo, T., Perez-Ruzafa, I.M., Flores-Moya, A., Conde, F., 1999. New collections of benthic marine algae from Livingston and Deception Islands (South Shetland Islands) and Trinity Island (Bransfield Strait) Antarctica. *Bot. Mar.* 42, 61–69.
- Garcia, A., Viramonte, J.G., Vila, J., Ibañez, J.M., 1989. Estudio del campo magnético en Port Foster (Isla Decepción). Final. Proc. III Symposium Español Estudios Antárticos. Gredos, Madrid, pp. 244–249.
- German, C.R., Baker, E.T., Klinkhammer, G., 1995. Regional setting of hydrothermal activity. In: Parson, L.M., Walker, C.L., Dixon, D.R. (Eds.), *Hydrothermal Vents and Processes*. Geological Society London, Special Publication 87, pp. 3–15.
- González-Casado, J.M., Giner-Robles, J.L., López-Martínez, J., 2000. Bransfield Basin, Antarctic Peninsula: Not a normal backarc basin. *Geology* 28, 1043–1046.
- González-Ferrán, O., 1985. Volcanic and tectonic evolution of the Northern Antarctic Peninsula – Late Cenozoic to Recent. *Tectonophysics* 114, 389–409.
- Gracia, E., Canals, M., Farrán, M.J., Prieto, M.J., Sorribas, J., Gebra Team, 1996. Morphostructure and evolution of the Central and Eastern Bransfield basins (NW Antarctic Peninsula). *Mar. Geophys. Res.* 18, 429–448.
- Hannington, M., Herzig, P., Stoffers, P., Scholten, J., Botz, R., Garbe-Schönberg, D., Jonasson, I.R., Roest, W., Shipboard Scientific Party, 2001. First observations of high-temperature submarine hydrothermal vents and massive anhydrite deposits of the north coast of Iceland. *Mar. Geol.* 177, 199–200.
- Humphris, S.E., Herzig, P.M., Miller, D.J., Alt, J.C., Becker, K., Brown, D. et al., 1995. The internal structure of an active sea-floor sulphide deposits. *Nature* 377, 713–716.
- Keller, R.A., Fisk, M.R., Smellie, J.L., Strelin, J.A., Lawver, L.A. 2002. Geochemistry of back-arc basin volcanism in Bransfield Strait, Antarctica: Subducted contributions and along axis variations. *J. Geophys. Res.* 107 (B8), 10.1029/2001JB000444.
- Klinkhammer, G.P., Elderfield, H., Hudson, A., 1983. Rare earth elements in seawater near hydrothermal vents. *Nature* 305, 185–188.
- Klinkhammer, G.P., Elderfield, H., Edmond, J.M., Mitra, A., 1994. Geochemical implications of rare earth element patterns in hydrothermal fluids from mid-ocean ridges. *Geochim. Cosmochim. Acta* 58, 5105–5113.
- Klinkhammer, G.P., Chin, C.S., Wilson, C., German, C.R., 1995. Venting from the Mid-Atlantic Ridge at 37°17'N: The Lucky Strike hydrothermal site. In: Parson, L.M., Walker, C.L., Dixon, D.R. (Eds.), *Hydrothermal Vents and Processes*. Geological Society London, Special Publication 87, pp. 87–96.
- Klinkhammer, G.P., Chin, C.S., Keller, R.A., Dählmann, A., Sahling, H., Sarthou Petersen, S., Smith, F., Wilson, C., 2001. Discovery of new hydrothermal vent sites in Bransfield Strait, Antarctica. *Earth Planet. Sci. Lett.* 193, 395–407.
- Lawver, L.A., Keller, R.A., Fisk, M.R., Strelin, J.A.S., 1995. Bransfield Strait, Antarctic Peninsula active extension behind a dead arc. In: Taylor, B. (Ed.), *Backarc Basins: Tectonics and Magmatism*. Plenum Press, New York, pp. 315–342.
- Lawver, L.A., Sloan, B.J., Barker, D.H.N., Ghidella, M., Von Herzen, R.P., Keller, R.A., Klinkhammer, G.P., Chin, C.S., 1996. Distributed, Active Extension in Bransfield Basin, Antarctic Peninsula: Evidence from Multibeam Bathymetry. *GSA Today* 6, 1–7.
- Lenn, Y., Chereskin, T., Smith, K., Glatts, R., Baldwin, R., Sturz, A., 2002. Seasonal variability in an Antarctic ecosystem of Deception Island. *Eos Transcr.* 83, 4.
- LeMasurier, W.E., Thomson, J.W. (Eds.), 1990. *Volcanoes of the Antarctic Plate and Southern Oceans*. Antarctic Research Series 48, American Geophysical Union, Washington, DC, 487 pp.
- Livermore, R., Balanyá, J.C., Maldonado, A., Martínez, J.M., Rodríguez-Fernández, J., Sanz de Galdeano, C., Galindo Zaldívar, J., Jabaloy, A., Barnolas, A., Somoza, L., Hernández-Molina, F.J., Suriñach, E., Viseras, C., 2000. Autopsy on a dead spreading centre: The Phoenix Ridge, Drake Passage, Antarctica. *Geology* 28, 607–610.
- López, J., Ramos, M., Criado, C., Serrano, E., Nicolás, P., 1995. Anomalías geotérmicas y permafrost en la Isla Decepción, Antártida. Final. Proc. V Simposio Estudios Antárticos, Madrid, pp. 223–242.
- López-Martínez, J., Serrano, E., 2002. Geomorphology. In: Smellie, J.L., López-Martínez, J., et al. (Eds.), *Geology and Geomorphology of Deception Island: Sheets 6-A and 6-B, 1:25000*. BAS GEOMAP Series, British Antarctic Survey, Cambridge, pp. 31–39.
- Massoth, G.J., Butterfield, D.A., Lupton, J.E., McDuff, R.E., Lilley, M.D., Jonasson, I.R., 1989. Submarine venting of phase-separated hydrothermal fluids at Axial Volcano, Juan de Fuca Ridge. *Nature* 340, 702–705.
- Morgan, J.W., Wandless, G.A., 1980. Rare earth element distribution in some hydrothermal minerals evidence crystallographic control. *Geochim. Cosmochim. Acta* 44, 973–980.
- Murton, B.J., Van Dover, C., Southward, E., 1995. Geological setting and ecology of the Broken Spur hydrothermal field: 29°10'N on the Mid-Atlantic Ridge. In: Parson, L.M., Walker, C.L., Dixon, D.R. (Eds.), *Hydrothermal Vents and Processes*. Geological Society London, Special Publication 87, pp. 33–42.
- Orheim, O., 1972. Volcanic activity on Deception Island, South Shetland Island, in: Adie, R.J. (Ed.), *Antarctic Geology and Geophysics*. Int. Union Geol. Sci., pp. 117–120.
- Ortiz, R., Vila, J., Garcia, A., Camacho, A.G., Diez, J.L., Aparicio, A., Soto, R., Viramonte, J.G., Riso, C., Menegatti, N., Petrinovic, I., 1992. Geophysical features of Deception Island. In: Yoshida et al. (Eds.), *Recent Progress in Antarctic Earth Science*. Terra Scientific Publications, Tokyo, pp. 443–448.
- Pankhurst, R.J., Smellie, J.L., 1983. K–Ar geochronology of the South Shetland Islands, Lesser Antarctica: Apparent lateral migration of Jurassic to Quaternary island arc volcanism. *Earth Planet. Sci. Lett.* 66, 214–222.
- Parson, L.M., Walker, C.L., Dixon, D.R. (Eds.), 1995. Hydro-

- thermal Vents and Processes. Geological Society London, Special Publication 87, London.
- Peccerillo, A., Tripodo, A., Villari, L., Gurrieri, S., Zimbalatti, E., 1991. Genesis and evolution of volcanism in back-arc areas: A case history, the island of Deception (Western Antarctica). *Per. Mineral.* 60, 29–44.
- Pelayo, A., Wiens, D., 1980. Stress in arc-back arc regions and plate subduction. *J. Geophys. Res.* 85, 6419–6428.
- Piper, D.Z., Graef, P.A., 1974. Gold and rare-earth elements in sediments from East Pacific Rise. *Mar. Geol.* 17, 287–297.
- Planke, S., Svensen, H., Jamveit, B., Podladtchikov, Y., 2002. Seeps and sediment volcanism in volcanic basins. Part II: Marine seismic and borehole analysis in the Voring and More Basins, Norway. Final Proc. VII Int. Conf. on Gas in Marine Sediments and Natural Hydrocarbon Marine Hydrocarbon Seepage in the World Oceans, Nafta-press, Baku, pp. 159–160.
- Ramos, M., Ortiz, R., Diez-Gil, J.L., Viramonte, J., 1989. Anomalías térmicas y balance de flujo energético sobre el suelo del volcán Decepción, Isla Decepción (Shetland del Sur). Final. Proc. III Symposium Español Estudios Antárticos, Gredos, pp. 203–219.
- Rey, J., Somoza, L., 1992. Neotectonic of extensional processes related to the Bransfield Rift, Deception Island (Antarctica). In: Mörner, N.A., Owen, L.A., Vita-Finzi, C. (Eds.), *Neotectonics—Recent Advances*. Quaternary Research Association, Cambridge, pp. 57–58.
- Rey, J., Maestro, A., Somoza, L., Smellie, J.L., 2002. Submarine morphology and seismic stratigraphy of Port Foster. In: Smellie, J.L., López-Martínez, J., et al. (Eds.), *Geology and Geomorphology of Deception Island*, Sheets 6-A and 6-B, 1:25 000. BAS GEOMAP Series, British Antarctic Survey, Cambridge, pp. 40–46.
- Rey, J., Somoza, L., Hernandez-Molina, F. J., 1992. Formas de los sedimentos submarinos superficiales en Puerto Foster, Isla Decepción, Islas Shetland del Sur. In: López-Martínez, J. (Ed.), *Geología de la Antártida Occidental*. Salamanca, pp. 163–172.
- Rey, J., Somoza, L., Martínez-Frías, J., 1995. Tectonic, volcanic and hydrothermal event sequence on Deception Island (Antarctica). *Geo-Mar. Lett.* 15, 1–8.
- Rey, J., Somoza, L., Martínez-Frías, J., Benito, R., Martín-Alfageme, S., 1997. Deception Island (Antarctica): A new target for exploration of Fe–Mn mineralization? In: Nicholson, K., Hein, J.R., Buhn, B., Dasgupta, S. (Eds.), *Manganese Mineralization: Geochemistry and Mineralogy of Terrestrial and Marine Deposits*. Geological Society London, Special Publication 119, pp. 239–251.
- Risso, C., Aparicio, A., 2002. Plutonic xenoliths in Deception Island. *Terra Antarctica* 9, 95–99.
- Roach, P.J., 1978. The nature of back-arc extension in Bransfield Basin (abst). *R. Astron. Soc. Geophys. J.* 53, 165.
- Schloesser, P., Suess, E., Bayer, R., Rheim, M., 1988. ^3He in the Bransfield Strait waters: Indication for local injection from back-arc rifting. *Deep-Sea Res.* 35, 1919–1935.
- Shultz, C.H., 1972. Eruption at Deception Island, Antarctica, August 1970. *GSA Bull.* 83, 2837–2842.
- Smellie, J.L., 1988. Recent observations on the volcanic history of Deception Island, South Shetland Islands. *Br. Antarct. Surv. Bull.* 81, 83–85.
- Smellie, J.L., 1990. Graham Land and South Shetland Islands: Summary. In: LeMasurier, W.E., Thomson, J.W. (Eds.), *Volcanoes of the Antarctic Plate and Southern Oceans*. American Geophysical Union, Washington, DC, pp. 303–312.
- Smellie, J.L., López-Martínez, J., 2000. Geological map of Deception Island. In: Smellie, J.L., López-Martínez, J., et al. (Eds.), *Geology and Geomorphology of Deception Island*, Sheet 6-A, 1:25 000. BAS GEOMAP Series, British Antarctic Survey, Cambridge.
- Smellie, J.L., 2001. Lithostratigraphy and volcanic evolution of Deception Island, South Shetland Islands. *Antarct. Sci.* 13, 188–209.
- Smellie, J.L., 2002a. The 1969 subglacial eruption on Deception Island (Antarctica): Events and processes during an eruption beneath a thin glacier and implications for volcanic hazards. In: Smellie, J.L., Chapman, M.G. (Eds.), *Volcano–Ice Interaction on Earth and Mars*. Geological Society London, Special Publication 202, pp. 59–79.
- Smellie, J.L., 2002b. Geology. In: Smellie, J.L., López-Martínez, J., et al. (Eds.), *Geology and geomorphology of Deception Island*, 78 pp., with accompanying maps. BAS GEOMAP Series, Sheets 6-A and 6-B, 1:25 000. Cambridge, British Antarctic Survey, pp. 11–30.
- Smellie, J.L., Hofstetter, A., Troll, G., 1992. Fluorine and boron geochemistry of an ensialic marginal basin volcano: Deception Island, Bransfield Strait, Antarctica. *J. Volcanol. Geotherm. Res.* 49, 255–267.
- Smellie, J.L., López-Martínez, J., et al. (Eds.), 2002. *Geology and Geomorphology of Deception Island*, Sheets 6-A and 6-B, 1:25 000. BAS GEOMAP Series, British Antarctic Survey, Cambridge.
- Suess, E., Fisk, M., Kadko, D., 1987. Thermal interaction between backarc volcanism and basin sediments in the Bransfield Strait, Antarctica. *Antarct. J. U.S.* 22, 46–49.
- Svensen, H., Jamveit, B., Planke, S., 2002. Seeps and sediment volcanism in volcanic basins. Final Proc. VII Int. Conf. on Gas in Marine Sediments and Natural Hydrocarbon Marine Hydrocarbon Seepage in the World Oceans, Nafta-press, Baku, pp. 199–200.
- Valentin, A., Martini, M., Diez-Gil, J.L., 1989. Geoquímica de fluidos en Isla Decepción. Final. Proc. III Symposium Español Estudios Antárticos, Gredos, pp. 195–202.
- Valenzuela, E., Chavez, B.L., Munizaga, V.F., 1968. Informe preliminar sobre la erupción de Isla Decepción ocurrida en Diciembre de 1967. *Bol. Inst. Antárt. Chil.* 3, 5–16.
- Vila, J., Martí, J., Ortíz, R., García, A., Correig, A.M., 1992. Volcanic tremors at Deception Island (South Shetland Islands, Antarctica). *J. Volcanol. Geotherm. Res.* 53, 89–102.
- Villegas, M.T., Caselli, A.T., 1995. Fumarolas de Decepción: Evolución a lo largo del Verano Austral. Final. Proc. 5th Symposium Español Estudios Antárticos, pp. 235–242.